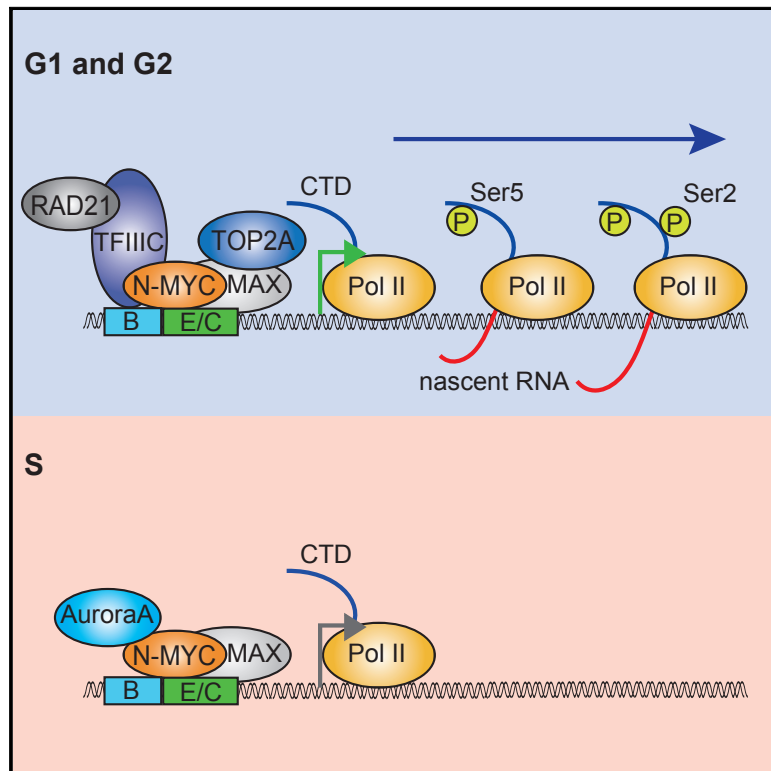Article

Association with Aurora-A Controls N-MYC-Dependent Promoter Escape and Pause Release of RNA Polymerase II during the Cell Cycle

Graphical Abstract

Authors
Gabriele Büchel, Anne Carstensen, Ka-Yan Mak, ..., Richard Bayliss, Susanne Walz, Martin Eilers

Correspondence
martin.eilers@biozentrum.uni-wuerzburg.de

In Brief
Büchel et al. demonstrate that N-MYC forms complexes with TFIIIC, TOP2A, and RAD21. Aurora-A competes with TFIIIC and RAD21 for binding to N-MYC, and Aurora-A displaces the three proteins from N-MYC during S phase. As consequence, N-MYC-dependent pause release is inhibited during S phase, preventing activation of the ATR checkpoint kinase.

Highlights
- N-MYC forms complexes with TFIIIC, RAD21, and TOP2A

- TFIIIC recruits RAD21 and is required for N-MYC-dependent pause release of Pol II

- Aurora-A displaces TFIIIC, TOP2A, and RAD21 from N-MYC during S phase

- Aurora-A inhibits pause release of Pol II during S phase

Data and Software Availability
GSE78957

CellPress

Article

Association with Aurora-A Controls N-MYC-Dependent Promoter Escape and Pause Release of RNA Polymerase II during the Cell Cycle

Gabriele Büchel,[1,9] Anne Carstensen,[1,9] Ka-Yan Mak,[1,9] Isabelle Roeschert,[1] Eoin Leen,[2,3] Olga Sumara,[1] Julia Hofstetter,[4] Steffi Herold,[1] Jacqueline Kalb,[1] Apoorva Baluapuri,[4] Evon Poon,[5] Colin Kwok,[5] Louis Chesler,[5] Hans Michael Maric,[6] David S. Rickman,[7] Elmar Wolf,[4] Richard Bayliss,[2,3] Susanne Walz,[8] and Martin Eilers[1,10,*]

[1]Theodor Boveri Institute and Comprehensive Cancer Center Mainfranken, Biocenter, University of Würzburg, Am Hubland, 97074 Würzburg, Germany
[2]Faculty of Biological Sciences, University of Leeds, Leeds LS2 9JT, UK
[3]University of Leicester, Leicester LE1 9HN, UK
[4]Cancer Systems Biology Group, Biochemistry and Molecular Biology, University of Würzburg, 97074 Würzburg, Germany
[5]Division of Clinical Studies and Cancer Therapeutics, The Institute of Cancer Research, The Royal Marsden NHS Trust, 15 Cotswold Rd., Belmont, Sutton, Surrey SM2 5NG, UK
[6]Department of Drug Design and Pharmacology, Center for Biopharmaceuticals, University of Copenhagen, Universitetsparken 2, 2100 Copenhagen, Denmark
[7]Weill Cornell Medicine, Sandra and Edward Meyer Cancer Center, 413 E. 69th Street, New York, NY 10021, USA
[8]Comprehensive Cancer Center Mainfranken, Core Unit Bioinformatics, Biocenter, University of Würzburg, Am Hubland, 97074 Würzburg, Germany
[9]These authors contributed equally
[10]Lead Contact
*Correspondence: martin.eilers@biozentrum.uni-wuerzburg.de
https://doi.org/10.1016/j.celrep.2017.11.090

SUMMARY

MYC proteins bind globally to active promoters and promote transcriptional elongation by RNA polymerase II (Pol II). To identify effector proteins that mediate this function, we performed mass spectrometry on N-MYC complexes in neuroblastoma cells. The analysis shows that N-MYC forms complexes with TFIIIC, TOP2A, and RAD21, a subunit of cohesin. N-MYC and TFIIIC bind to overlapping sites in thousands of Pol II promoters and intergenic regions. TFIIIC promotes association of RAD21 with N-MYC target sites and is required for N-MYC-dependent promoter escape and pause release of Pol II. Aurora-A competes with binding of TFIIIC and RAD21 to N-MYC *in vitro* and antagonizes association of TOP2A, TFIIIC, and RAD21 with N-MYC during S phase, blocking N-MYC-dependent release of Pol II from the promoter. Inhibition of Aurora-A in S phase restores RAD21 and TFIIIC binding to chromatin and partially restores N-MYC-dependent transcriptional elongation. We propose that complex formation with Aurora-A controls N-MYC function during the cell cycle.

INTRODUCTION

The MYC family of transcription factors (MYC, N-MYC, and L-MYC) has been causally implicated in the development of mul-

tiple human tumors (Dang, 2012). MYC proteins bind to virtually all promoters with an open chromatin structure as well as to thousands of enhancers (Walz et al., 2014; Sabò et al., 2014; Lin et al., 2012; Nie et al., 2012). They stimulate transcription of large groups of genes encoding, among others, proteins involved in protein translation, cell cycle progression, and intermediary metabolism and repress transcription of genes encoding cell cycle inhibitory proteins as well as proteins involved in cell adhesion and differentiation (Dang, 2012). In some settings, MYC proteins act as "general amplifiers" that enhance transcription of all actively transcribed protein-coding genes (Nie et al., 2012; Lin et al., 2012).

During early transcription, RNA polymerase II (Pol II) goes through a series of intermediate states that begin with the formation of a closed promoter complex and end with the release of Pol II from a promoter-proximal pause position into productive elongation (Michel and Cramer, 2013). To enhance transcription, MYC proteins promote both recruitment of Pol II to the promoter and its subsequent release into elongation (Rahl et al., 2010; Jaenicke et al., 2016; Walz et al., 2014). Escape from the promoter and pause release of Pol II are controlled by sequential phosphorylation of Ser5 and Ser2 in the C-terminal domain of Pol II and activation of MYC promotes phosphorylation at both sites (Jonkers and Lis, 2015; Rahl et al., 2010; Walz et al., 2014; Cowling and Cole, 2007). Known protein-protein interactions of MYC include the association with MAX, which is required for binding to DNA (Blackwell et al., 1993), the NuA4 histone acetylase complex (McMahon et al., 1998), the p400 and BPTF chromatin-remodeling complexes (Richart et al., 2016; Fuchs et al., 2001), and the PAF1C elongation complex (Jaenicke et al., 2016). How MYC engages its different

cofactors to promote elongation and how this process is regulated is largely unknown.

Deregulated expression of N-MYC is characteristic for subentities of pediatric neuroblastoma and medulloblastoma as well as for adult neuroendocrine and some hematopoietic malignancies (Beltran, 2014). Like all MYC proteins, N-MYC is rapidly turned over via the ubiquitin/proteasome system (Sjostrom et al., 2005). The SCF^{FBXW7} ubiquitin ligase recognizes a phosphodegron that is part of a conserved domain called MYCBoxI (Welcker et al., 2004). Replacing two phosphoresidues, T58 and S62, with alanine stabilizes N-MYC (Otto et al., 2009). S62 is phosphorylated by cyclin-dependent kinases and primes phosphorylation of T58 by GSK3, resulting in cell cycle- and growth factor-dependent proteasomal turnover of N-MYC (Chesler et al., 2006; Sjostrom et al., 2005).

In multiple tumor entities, N-MYC is stabilized by complex formation with Aurora-A (Otto et al., 2009; Dardenne et al., 2016). Aurora-A is a serine/threonine kinase that is best known for its role in centrosome function and mitosis (Marumoto et al., 2005). Aurora-A binds to N-MYC directly via two domains that flank the SCF^{FBXW7} phosphodegron and antagonizes degradation of N-MYC by SCF^{FBXW7} (Otto et al., 2009; Richards et al., 2016). Although stabilization of N-MYC does not require Aurora-A catalytic activity, Aurora-A inhibitors that distort the kinase domain dissociate the N-MYC/Aurora-A complex and destabilize N-MYC (Richards et al., 2016). These inhibitors show therapeutic efficacy in N-MYC-driven tumor models and are being tested in human patients (DuBois et al., 2016). We have now analyzed protein complexes of N-MYC to understand how N-MYC controls Pol II function and how association with Aurora-A impacts N-MYC function.

RESULTS

Complexes of N-MYC with TFIIIC, TOP2A, and RAD21

To identify protein complexes of N-MYC in neuroblastoma cells, we used SH-EP cells, which do not express endogenous N-MYC. Using retroviral infection, we stably expressed HA-tagged wild-type (WT) N-MYC (N-MYC$_{wt}$) or N-MYCT58AS62A (N-MYC$_{mut}$) (Figure 1A). Immunoblots showed that levels of N-MYC in infected cells were comparable with those found in a *MYCN*-amplified neuroblastoma cell line, IMR-32 (Figure 1A). We then performed mass spectrometry of complexes recovered after immunoprecipitation with α-hemagglutinin (α-HA) antibodies and elution with a HA peptide using label-free quantification (Figure 1B; Table S1). The analysis confirmed multiple well-validated interactions of N-MYC or MYC proteins, including interactions with TRRAP, p400, BPTF, MAX, Aurora-A, and CDC73 (Figure S1A). In addition, the analysis identified interactions with 5 of 6 subunits of the TFIIIC complex and topoisomerases IIA and IIB (TOP2A and TOP2B). TFIIIC is both a general transcription factor of RNA polymerase III and an architectural protein that is localized at the border of topological domains (Crepaldi et al., 2013; Van Bortle et al., 2014). TOP2A has been implicated in relieving transcription-induced supercoiling at highly active promoters (Kouzine et al., 2013). We speculated, therefore, that these interactions may identify effector functions of N-MYC.

Immunoprecipitations using α-HA antibodies confirmed that TFIIIC and TOP2A were present in immunoprecipitates from cells expressing N-MYC but not in control immunoprecipitates from cells not expressing HA-tagged N-MYC (Figure S1B). Parallel mass spectrometry demonstrated the presence of 5 of 6 subunits of TFIIIC and TOP2A in α-N-MYC immunoprecipitates but not in control immunoprecipitates from *MYCN*-amplified neuroblastoma cells (Figure S1C). Multiple subunits of TFIIIC and TOP2A were also detected in α-HA precipitates from U2OS cells expressing HA-tagged MYC but not control immunoprecipitates, arguing that MYC, like N-MYC, associates with these proteins (Figure S1D); this is consistent with a previous mass spectrometric analysis (Koch et al., 2007). Using an antibody that recognizes TFIIIC5, we confirmed that TFIIIC associates with endogenous N-MYC and, albeit more weakly, with TOP2A as well as TOP2B in *MYCN*-amplified neuroblastoma cells (Figure 1C; Figure S1E). Notably, interactions of N-MYC with TFIIIC5 and TOP2A were also observed in the presence of ethidium bromide (EtBr), which disrupts DNA-dependent interactions (Figure 1C). This observation precludes the possibility that the interactions are indirectly mediated by DNA.

To identify domains of N-MYC that interact with TFIIIC and TOP2A, we performed pull-down assays from cell lysates incubated with recombinant FLAG-tagged peptides covering fragments of the N-MYC N terminus (Figure 1D). These assays showed that residues 1–137 are sufficient for binding to TFIIIC and suggested that two regions of N-MYC that flank MYCBoxI, but not MYCBoxI itself (peptides 46–89), mediate binding to TFIIIC. Controls established that an equimolar amount of an unrelated FLAG-tagged protein (heterogeneous nuclear ribonucleoprotein [hnRNP], amino acids 330–463) does not bind TFIIIC5 (E.L., unpublished data). In parallel assays, we were unable to demonstrate that residues 1–137 of N-MYC are sufficient for binding to TOP2A (E.L., unpublished data). Previous work has demonstrated that TFIIIC co-localizes and associates with cohesin and condensin complexes in different organisms (Van Bortle et al., 2014; D'Ambrosio et al., 2008), prompting us to search for the presence of these complexes in N-MYC immunoprecipitates. Indeed, peptides of the kleisin component of the cohesin complex, RAD21, were found in the mass spectrometry analysis (Table S1), and we confirmed that both N-MYC expressed in SH-EP cells and endogenous N-MYC in *MYCN*-amplified IMR-5 cells associates with RAD21 (Figure 1E; Figure S1B). Mapping of the interaction to the N-MYC N terminus showed the same binding pattern as TFIIIC, suggesting that they co-exist with N-MYC in the same complex (Figure 1D).

Like TFIIIC and RAD21, Aurora-A interacts with N-MYC via two domains flanking MYCBoxI (Richards et al., 2016), raising the possibility that Aurora-A competes with TFIIIC or RAD21 for binding to N-MYC. Indeed, Aurora-A competed with both TFIIIC and RAD21 for binding to the N-MYC N terminus (1–137) in pull-down assays using FLAG-tagged peptides, whereas an equimolar amount of an unrelated protein, glutathione-S-transferase, did not compete (Figure 1F). Immunoprecipitations from *MYCN*-amplified neuroblastoma cells showed that TFIIIC, RAD21, and Aurora-A were present in α-N-MYC immunoprecipitates (Figure 1E). In parallel assays, both N-MYC and, weakly, TFIIIC, but not RAD21, were detectable in α-Aurora-A
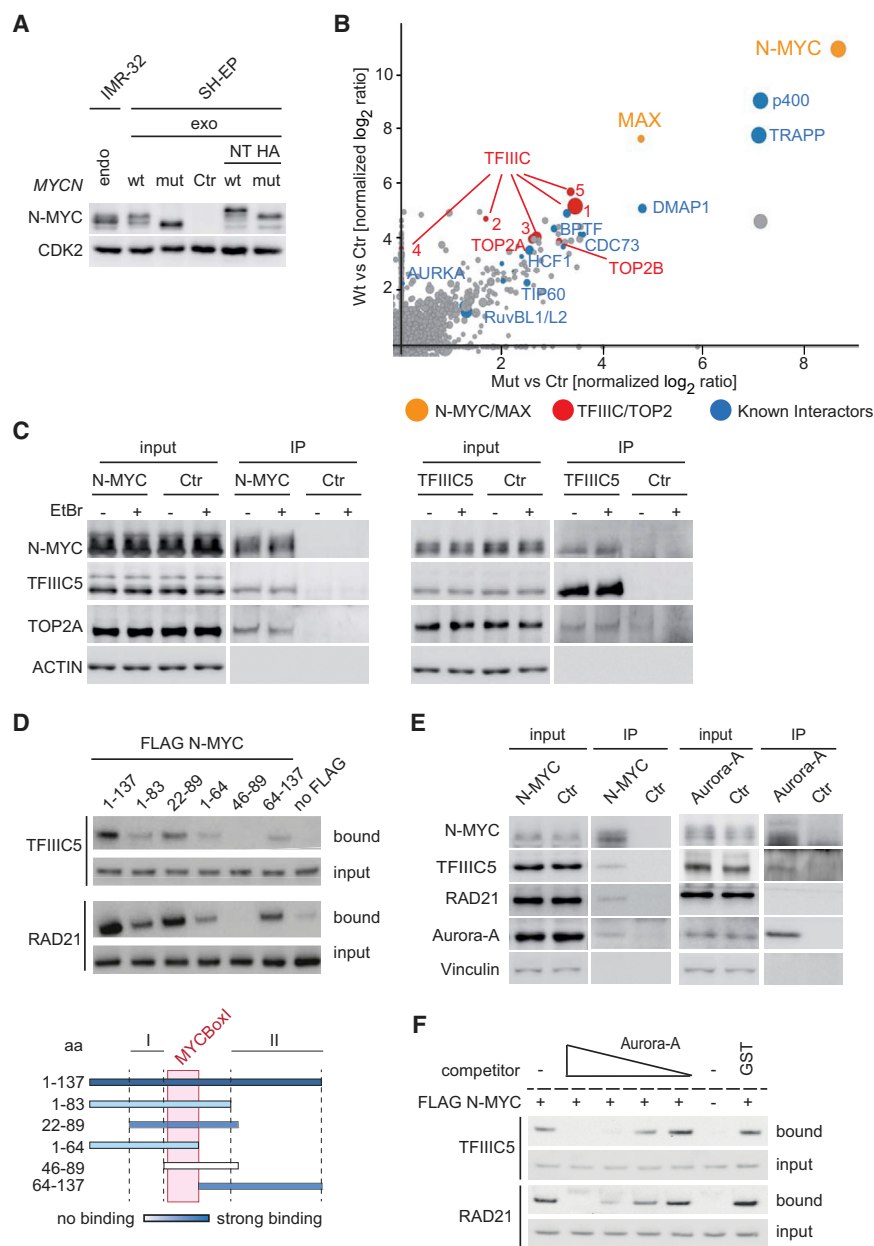
Figure 1. Complexes of N-MYC with TFIIIC, TOP2A, RAD21, and Aurora-A

(A) Immunoblot documenting levels of ectopically expressed (exo) N-MYC$_{wt}$ and N-MYC$_{mut}$ proteins in stably infected SH-EP neuroblastoma cells relative to endogenous N-MYC (endo) of IMR-32 *MYCN*-amplified neuroblastoma cells. Where indicated, ectopically expressed proteins carry an N-terminal HA tag (NT HA); hence, their molecular weight is slightly larger than that of the endogenous protein (n = 2).

(B) Results of mass spectrometry of α-HA immunoprecipitates of N-MYC$_{wt}$ and N-MYC$_{mut}$ complexes. The axes show the normalized ratio of peptides recovered in an α-HA immunoprecipitation from cells expressing N-MYC$_{wt}$ or N-MYC$_{mut}$ relative to an α-HA immunoprecipitation (IP) from control cells. Dot size represents the MaxQuant protein scores, which indicates the reliability of protein identification (Cox and Mann, 2008).

(C) Immunoblots of α-N-MYC (left) and α-TFIIIC5 (right) immunoprecipitates from IMR-32 cells. The input corresponds to 1% of the amount used for the precipitation. Where indicated, ethidium bromide (EtBr) was added to a final concentration of 1 μg ml^{-1} to disrupt DNA-dependent interactions. Non-specific immunoglobulin G (IgG) was used for control immunoprecipitations (n = 3).

(D) Pull-down assays from cell lysates documenting binding of TFIIIC5 and RAD21 to FLAG-tagged peptides spanning the indicated amino acids of the N-MYC N terminus. The input corresponds to 0.6% of the amount used for the precipitation (n = 2). The graph at the bottom visualizes the binding of the different N-MYC peptides. I/II indicate N-MYC sequences that mediate binding.

(E) Immunoblots of α-N-MYC (left) and α-Aurora-A (right) immunoprecipitates from *MYCN*-amplified IMR-5 cells. The input corresponds to 1% of the amount used for the precipitation. Non-specific IgG was used for control immunoprecipitates (n = 4).

(F) Pull-down assays from cell lysates documenting binding of TFIIIC5 and RAD21 to FLAG-tagged N-MYC peptides spanning amino acids 1–137 upon competition with Aurora-A. Recombinant Aurora-A protein was added in a concentration-dependent manner from 0.25 to 5 molar equivalents (Aurora-A/N-MYC peptide). 5 molar equivalents of glutathione-S-transferase (GST) were used as a control (n = 3).

See also Figure S1 and Table S1. n indicates the number of independent biological replicas for each experiment.

immunoprecipitates (Figure 1E). We concluded that Aurora-A and RAD21 form alternate complexes with N-MYC in cells, whereas Aurora-A can remain associated with N-MYC and TFIIIC via interactions that are outside of residues N-MYC 1–137 *in vivo*. To identify these domains in N-MYC, we used overlapping peptide libraries in microarray format of N-MYC and probed them with recombinant Aurora-A. Consistent with these and previously published data (Richards et al., 2016), peptides spanning amino acids 17–43 of N-MYC (9–43 in MYC) had the highest affinity for Aurora-A. The arrays also revealed an

additional binding site with lower binding affinity for Aurora-A in the C terminus of N-MYC, which spans amino acids 313–339 (overlapping MYCBoxIV) and is conserved in MYC (amino acids 306–331) (Figure S1F).

The interaction of Aurora-A with N-MYC is impaired by mutations of T58 and S62 in N-MYC to alanine (Otto et al., 2009), and immunoprecipitations from infected SH-EP cells confirmed this observation (Figure S1B). Comparison of precipitates recovered from cells expressing N-MYC$_{wt}$ with those from cells expressing N-MYC$_{mut}$ suggested that phosphorylation of MYCBoxI may
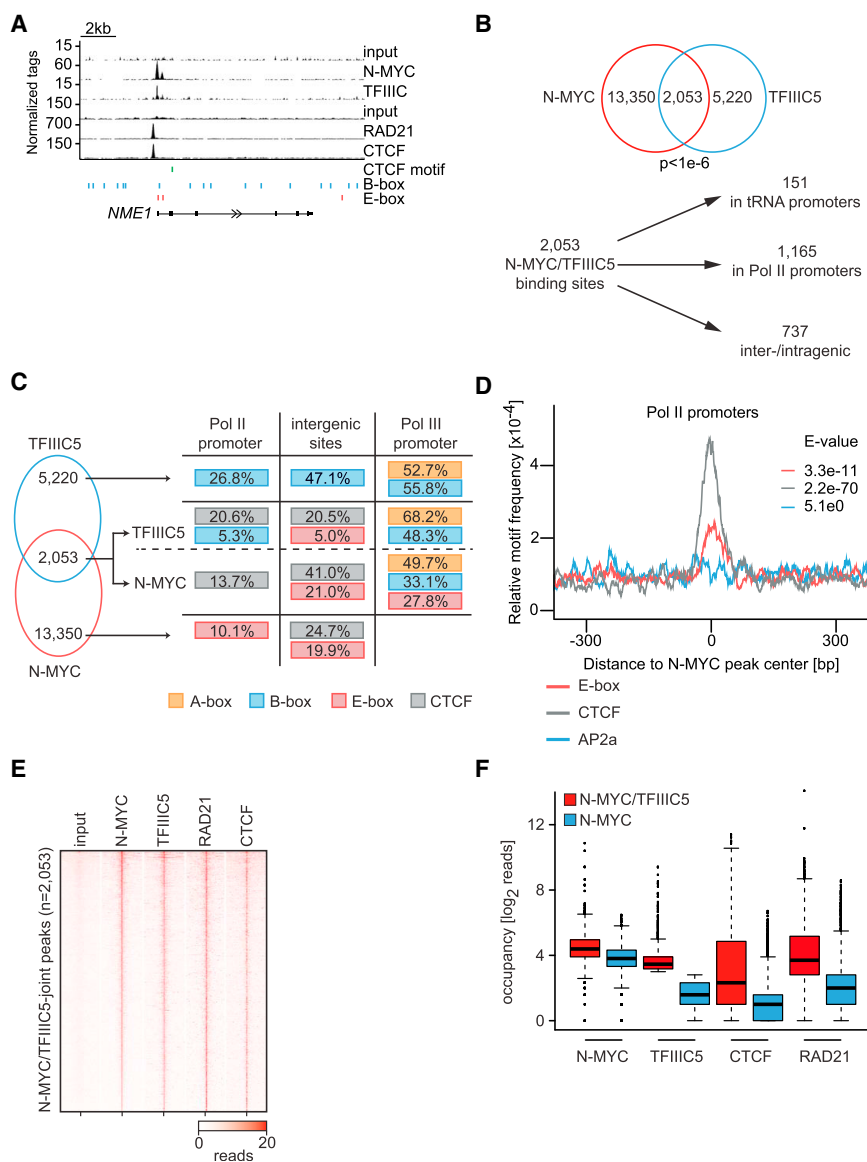
Figure 2. Chromatin Binding of N-MYC/TFIIIC Complexes

(A) Genome browser tracks at the *NME1* locus illustrating chromatin association of the indicated proteins. The positions of B- and E-boxes and of CTCF motifs are indicated by vertical lines. The upper input is for ChIP sequencing of N-MYC and TFIIIC5; the lower input is for RAD21 and CT*CF*.

(B) Top: Venn diagram documenting genome-wide overlap of N-MYC and TFIIIC5 binding sites in IMR-5 neuroblastoma cells. The p value was calculated using a permutation test. Bottom: diagram showing the location of N-MYC/TFIIIC5 sites in the genome.

(C) *De novo* motif search in N-MYC- and/or TFIIIC5-bound regions. In overlapping sites, both peak regions were analyzed. The numbers indicate the percentage of sites in which the indicated motif was found. E values for enrichment of the respective motif are shown in Figure S2D. Motifs are only shown if the enrichment was significant.

(D) Central enrichment of E-box, CTCF, and AP2a (as a negative control) motifs in the N-MYC peak of N-MYC/TFIIIC5 joint sites in Pol II promoters. The E value is calculated by a binominal test and adjusted for the number of motifs tested.

(E) Heatmap showing occupancy of N-MYC, TFIIIC5, RAD21, and CTCF on overlapping N-MYC/TFIIIC sites in IMR-5 cells. Samples are normalized to the same number of mapped reads, and peaks are sorted according to N-MYC binding.

(F) Boxplot documenting occupancy of the indicated proteins at joint N-MYC/TFIIIC5 binding sites (n = 1,630) and at N-MYC binding sites lacking TFIIIC5 (n = 2,406) located in promoters of Pol II genes. The number of reads was counted in a region of ± 100 bp around the N-MYC peak summit.

See also Figure S2. n indicates the number of independent biological replicas for each experiment.

affect the interaction with TFIIIC (Figure 1B), but immunoprecipitations from SH-EP cells did not reveal significant differences in the interactions of N-MYC$_{wt}$ and N-MYC$_{mut}$ with RAD21, TFIIIC5, and TOP2A (Figure S1B).

Joint N-MYC/TFIIIC Chromatin Binding Sites

TFIIIC binds to promoters transcribed by RNA polymerase III and is an architectural protein complex that binds to thousands of ETC (extra TFIIIC) sites throughout the genome that are independent of RNA polymerase III (Moqtaderi et al., 2010; Oler et al., 2010). To understand whether N-MYC and TFIIIC bind to overlapping sites on chromatin, we performed chromatin immunoprecipitation (ChIP) coupled with high-throughput sequencing (ChIP sequencing) using antibodies directed against N-MYC and TFIIIC5. Inspection of individual genes revealed the presence of both proteins in close vicinity to each other at multiple

transcription start sites (Figure 2A; Figure S2A). Global analyses identified a total of 2,053 sites with overlapping peaks, and statistical analyses showed that this overlap is highly significant (Figure 2B) (p < 10^{-6}, calculated using a permutation test with 1.0 × 10^6 iterations). The median distance between peak summits at all joint sites was 39 bp (Figure S2B). Of these sites, 151 were found at tRNA genes; this is expected because MYC proteins bind to tRNA genes (Gomez-Roman et al., 2003). In addition, overlapping N-MYC/TFIIIC binding sites were found at 1,165 promoters transcribed by Pol II and at 737 intra- and intergenic sites. At core promoters transcribed by Pol II, N-MYC binding peaked at transcription start sites, and TFIIIC binding peaked with a slightly larger median distance of 80 bp 5′ of N-MYC binding sites, suggesting that joint sites may have a defined orientation (Figure S2C).

MYC proteins bind to E-box sequences (CAC(A/G)TG) as part of a heterodimeric complex with MAX (Blackwell et al., 1993). Consistently, a *de novo* motif search identified E-boxes as a

predominant motif enriched in N-MYC binding sites in Pol II promoters and at N-MYC/TFIIIC joint intergenic sites (Figure 2C; Figure S2D). TFIIIC promotes binding to a sequence termed A-box at tRNA promoters that are not present at ETC sites (Figure 2C; Figure S2D; Moqtaderi et al., 2010). In addition, TFIIIC binds to a sequence termed B-box that is present in tRNA promoters and in ETC sites and the *de novo* motif search confirmed these observations (Figure 2C; Figure S2D; Moqtaderi et al., 2010). B-boxes were also found in overlapping N-MYC/TFIIIC sites in core promoters.

In addition to TFIIIC, ETC sites are also bound by the CTCF transcription factor (Moqtaderi et al., 2010; Oler et al., 2010; Carrière et al., 2012; Vietri Rudan and Hadjur, 2015). Indeed, a *de novo* motif search analysis identified a centrally enriched consensus motif for CTCF at joint N-MYC/TFIIIC binding sites (Figures 2C and 2D; Figures S2D–S2F). ChIP sequencing confirmed the presence of CTCF at 936 of 2,053 joint N-MYC/TFIIIC binding sites and showed a much lower occupancy at N-MYC sites that do not bind TFIIIC (Figures 2E and 2F; Figure S2G). We concluded that N-MYC is present at previously characterized TFIIIC binding sites both in RNA polymerase III promoters and at ETC sites.

N-MYC and TFIIIC Promote Chromatin Association of RAD21 at Joint Binding Sites

CTCF binding sites define contact points for RAD21/cohesin-mediated chromosomal interactions (Ghirlando and Felsenfeld, 2016). Consistent with this notion, ChIP sequencing showed that RAD21 was present at virtually all (22,642 of 23,479) CTCF-bound sites and at 1,328 of 2,053 joint N-MYC/TFIIIC sites (Figures 2E and 3A). RAD21 occupancy was much lower at N-MYC sites that do not bind TFIIIC (Figure 2F). We also observed that endogenous TFIIIC5 robustly co-immunoprecipitated endogenous RAD21 (Figure 3B). Because RAD21/cohesin complexes do not bind DNA directly, these observations raised the question of whether TFIIIC or N-MYC affects chromatin association of each other and of RAD21. We therefore performed ChIP experiments in cells stably expressing doxycycline-inducible short hairpin RNAs (shRNAs) targeting either TFIIIC or N-MYC. Depletion of TFIIIC5 had little effect on steady-state levels of N-MYC, RAD21, Aurora-A, and the DNA binding subunit TFIIIC2 but led to a small reduction in TFIIIC1 levels (Figure 3C; Figure S3A; Shen et al., 1996). As expected, we observed reduced binding of TFIIIC5 at multiple N-MYC-bound loci (Figure 3D). Depletion of TFIIIC5 had no effect on binding of N-MYC but reduced binding of RAD21 at almost all tested joint binding sites, demonstrating that TFIIIC5 promotes binding of RAD21 (Figure 3D). In contrast, depletion of TFIIIC5 had no effect on RAD21 association with sites that were not bound by TFIIIC and N-MYC (Figure S3B). Notably, shRNA-mediated depletion of TFIIIC5 strongly reduced TFIIIC5 occupancy at sites transcribed by Pol II, but TFIIIC5 binding to tRNA sites was more stable (Figure S3C). Although RAD21 is not detected at tRNA genes (Oler et al., 2010; Moqtaderi et al., 2010), the stable binding of TFIIIC5 to tRNA encoding genes precluded an unequivocal determination of whether TFIIIC5 promotes binding of N-MYC to tRNA genes. We also depleted TFIIIC2 and found that this has no effect on either N-MYC or RAD21 binding to joint sites,

arguing that not all subunits of TFIIIC are limiting for chromatin association of RAD21 (Figures S3A and S3D). Depletion of N-MYC using a doxycycline-inducible shRNA reduced binding of N-MYC to most joint sites and significantly reduced binding of both TFIIIC5 and of RAD21 to some sites, although the extent of reduction was more variable than observed after TFIIIC5 depletion (Figures 3E and 3F). In contrast, depletion of N-MYC did not decrease RAD21 association with sites that were not bound by TFIIIC and N-MYC (Figure S3E). Taken together, the results suggest a hierarchy of chromatin binding in which N-MYC contributes to recruitment of both TFIIIC5 and RAD21 and TFIIIC5 is required for association of RAD21 with joint binding sites.

Transcriptional Regulation by N-MYC and TFIIIC/RAD21

To determine whether TFIIIC5 and RAD21 are required for the transcription of N-MYC target genes, we depleted either protein in IMR-5 cells using specific siRNAs. Control immunoblots are shown in Figure 4A. RNA sequencing of two independent samples for each protein showed a significant overlap of genes regulated in response to depletion of either protein (Figure 4B). Gene set enrichment analysis (GSEA) (Subramanian et al., 2005) showed that multiple well-characterized sets of MYC-activated target genes were significantly downregulated upon depletion of TFIIIC5 or RAD21; in contrast, only few gene sets were significantly upregulated upon depletion of TFIIIC5 or RAD21 (Figures 4C and 4D). GSEA showed that the most consistently downregulated gene sets encoded proteins involved in cell cycle progression, DNA replication, nucleotide metabolism, and telomere biology (Figure 4D). Comparison with expression profiles obtained after shRNA-mediated depletion of N-MYC in neuroblastoma cells (Valentijn et al., 2012) confirmed that expression of these genes is sensitive to depletion of N-MYC (Figures 4C and 4E). Furthermore, expression of gene sets that are sensitive to depletion of TFIIIC, RAD21, and N-MYC strongly correlated with *MYCN* amplification and advanced tumor stage in neuroblastoma, both of which are characteristic features of aggressive tumors with a poor prognosis (Figure 4F; Molenaar et al., 2012). We concluded that TFIIIC and RAD21 are required for expression of a subset of N-MYC target genes that are characteristic for *MYCN*-amplified neuroblastoma tumors. Consistent with these effects on gene expression, shRNA-mediated depletion of TFIIIC5 protein suppressed the growth of neuroblastoma cells (Figure S4A), although it had little effect on the expression of two tRNA genes we tested (Figure S4B). Notably, growth suppression by depletion of TFIIIC5 was independent of *MYCN* amplification (Figure S4A), arguing that TFIIIC5 also has essential functions in non *MYCN*-amplified cells. Most likely, the residual growth of IMR-5 cells after shRNA-mediated depletion of TFIIIC5 was due to incomplete removal of TFIIIC5 because multiple sgRNAs targeting TFIIIC5 eliminated cell growth (Figure S4C). This is consistent with the demonstration that subunits 1–5 of TFIIIC, RAD21, and TOP2A have been identified as essential proteins in genome-wide CRISPR-based loss-of-function screens (Hart et al., 2015). Depletion of TFIIIC5 caused little apoptosis and, like depletion of N-MYC (Otto et al., 2009), delayed progression through all phases of the
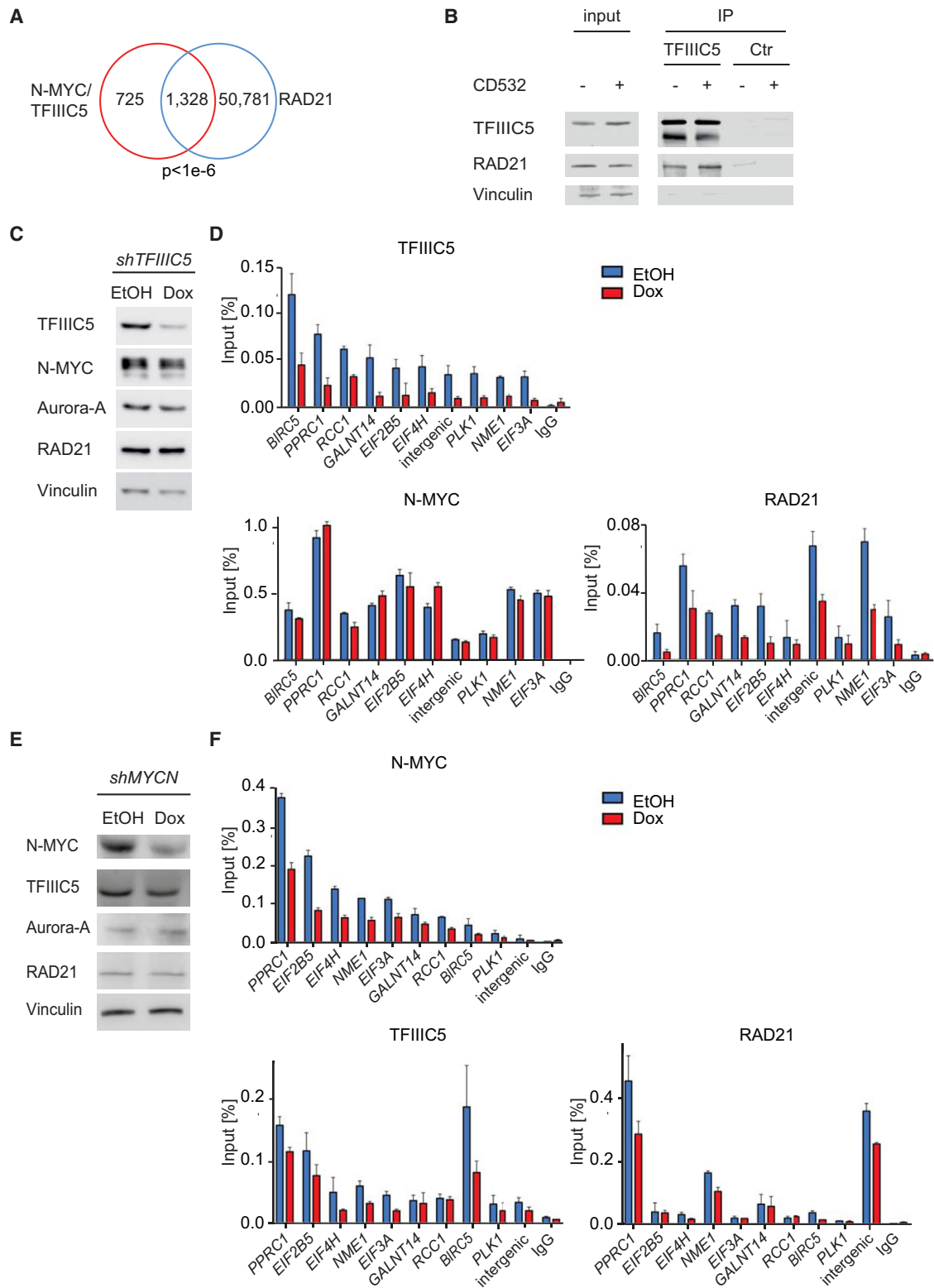
Figure 3. Assembly of N-MYC/TFIIIC and RAD21 Complexes on Chromatin

(A) Venn diagram documenting genome-wide overlap of N-MYC/TFIIIC5 joint binding sites with RAD21 binding sites. The p value was calculated using a permutation test with 100,000 iterations.
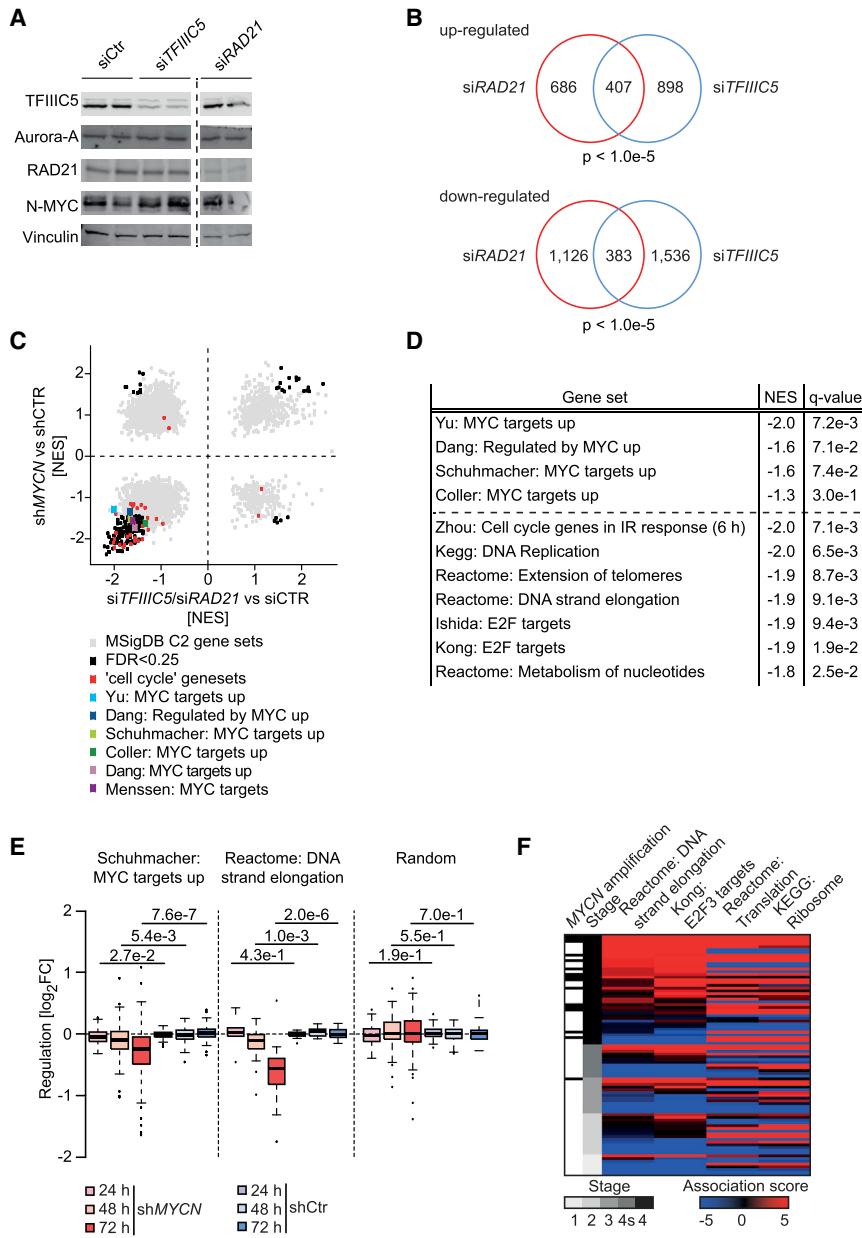
(legend continued on next page)

A

	siCtr	siTFIIIC5	siRAD21
TFIIIC5			
Aurora-A			
RAD21			
N-MYC			
Vinculin			

B

up-regulated

siRAD21 686 407 898 siTFIIIC5

p < 1.0e-5

down-regulated

siRAD21 1,126 383 1,536 siTFIIIC5

p < 1.0e-5

C

sh*MYCN* vs shCTR [NES]

si*TFIIIC5*/si*RAD21* vs siCTR [NES]

- ■ MSigDB C2 gene sets
- ■ FDR<0.25
- ■ 'cell cycle' genesets
- ■ Yu: MYC targets up
- ■ Dang: Regulated by MYC up
- ■ Schuhmacher: MYC targets up
- ■ Coller: MYC targets up
- ■ Dang: MYC targets up
- ■ Menssen: MYC targets

D

Gene set	NES	q-value
Yu: MYC targets up	-2.0	7.2e-3
Dang: Regulated by MYC up	-1.6	7.1e-2
Schuhmacher: MYC targets up	-1.6	7.4e-2
Coller: MYC targets up	-1.3	3.0e-1
Zhou: Cell cycle genes in IR response (6 h)	-2.0	7.1e-3
Kegg: DNA Replication	-2.0	6.5e-3
Reactome: Extension of telomeres	-1.9	8.7e-3
Reactome: DNA strand elongation	-1.9	9.1e-3
Ishida: E2F targets	-1.9	9.4e-3
Kong: E2F targets	-1.9	1.9e-2
Reactome: Metabolism of nucleotides	-1.8	2.5e-2

E

Schuhmacher: MYC targets up; Reactome: DNA strand elongation; Random

Regulation [log₂FC]

□ 24 h ■ 48 h ■ 72 h | sh*MYCN*
□ 24 h ■ 48 h ■ 72 h | shCtr

F

MYCN amplification; Stage; Reactome: DNA strand elongation; Kong: E2F3 targets; Reactome: Translation; KEGG: Ribosome

Stage 1 2 3 4s 4

Association score -5 0 5

Figure 4. Gene Regulation by N-MYC, TFIIIC, and RAD21

(A) Immunoblots documenting levels of the indicated proteins 48 hr after transfection of specific siRNAs. Duplicate samples are shown, both of which were used for RNA sequencing. All lanes are from the same exposure of a single immunoblot.

(B) Venn diagrams documenting the overlap of upregulated (top) and downregulated (bottom) genes after depletion of TFIIIC5 or RAD21 in IMR-5 neuroblastoma cells. The p values were calculated using a Monte Carlo simulation with 100,000 permutations and all expressed genes (n = 17,450) as the basis.

(C) Correlation of gene sets that change in expression upon depletion of N-MYC with the aggregate of changes in response to siRNA-mediated depletion of RAD21 and TFIIIC5. Each dot reflects a gene set. A light gray color indicates that the expression change of a gene set was not statistically significant. Published sets of MYC target genes are colored.

(D) Examples of gene sets that are downregulated in response to depletion of both RAD21 and TFIIIC5. NES is the normalized enrichment score, indicating direction and extent of regulation.

(E) Boxplots documenting changes in expression of selected gene sets upon depletion of N-MYC using a Dox-inducible shRNA in IMR-32 neuroblastoma cells.

(F) Heatmap illustrating stage-specific expression of N-MYC/TFIIIC/RAD21-regulated genes sets in human neuroblastoma cells. The black bars in the first row indicate *MYCN* amplification status.

See also Figure S4. n indicates the number of independent biological replicas for each experiment.

Cell Cycle-Dependent Regulation of N-MYC Binding and Chromatin Association

Aurora-A has been implicated in cell cycle progression, prompting us to analyze complex formation between N-MYC and Aurora-A throughout the cell cycle in a semiquantitative manner using proximity ligation assays (PLAs) (Söderberg et al., 2006). In PLAs, a rolling circle amplification using oligonucleotides bound to secondary antibodies generates a signal that appears as a fluorescent dot when two antigens are in proximity of each other. Controls using a N-MYC

cell cycle; hence, fluorescence-activated cell sorting (FACS) analyses did not detect a major shift in cell cycle distribution (Figure S4D).

(B) Immunoblots of α-TFIIIC5 immunoprecipitates from IMR-5 cells. The input corresponds to 1% of the amount used for the precipitation. Non-specific IgG was used for control immunoprecipitates. Where indicated, CD532 (1 μM) was added to cells 4 hr prior to immunoprecipitation (n = 3).

(C) Immunoblot showing levels of the indicated proteins in response to depletion of TFIIIC5. IMR-5 cells expressing an inducible shRNA directed against TFIIIC5 were treated with doxycycline (Dox) for 48 hr or with ethanol (EtOH) as a control (n = 3).

(D) ChIP experiments documenting binding of TFIIIC5, N-MYC, and RAD21 to the indicated loci upon depletion of TFIIIC5. Error bars show SD of technical triplicates from one experiment (n = 2).

(E) Immunoblot showing levels of the indicated proteins in response to depletion of N-MYC. IMR-5 cells expressing an inducible shRNA directed against N-MYC were treated with Dox for 48 hr or with EtOH as a control (n = 3).

(F) ChIP experiments documenting binding of TFIIIC5, N-MYC, and RAD21 to the indicated loci upon depletion of N-MYC. Error bars show SD of technical triplicates from one experiment (n = 2).

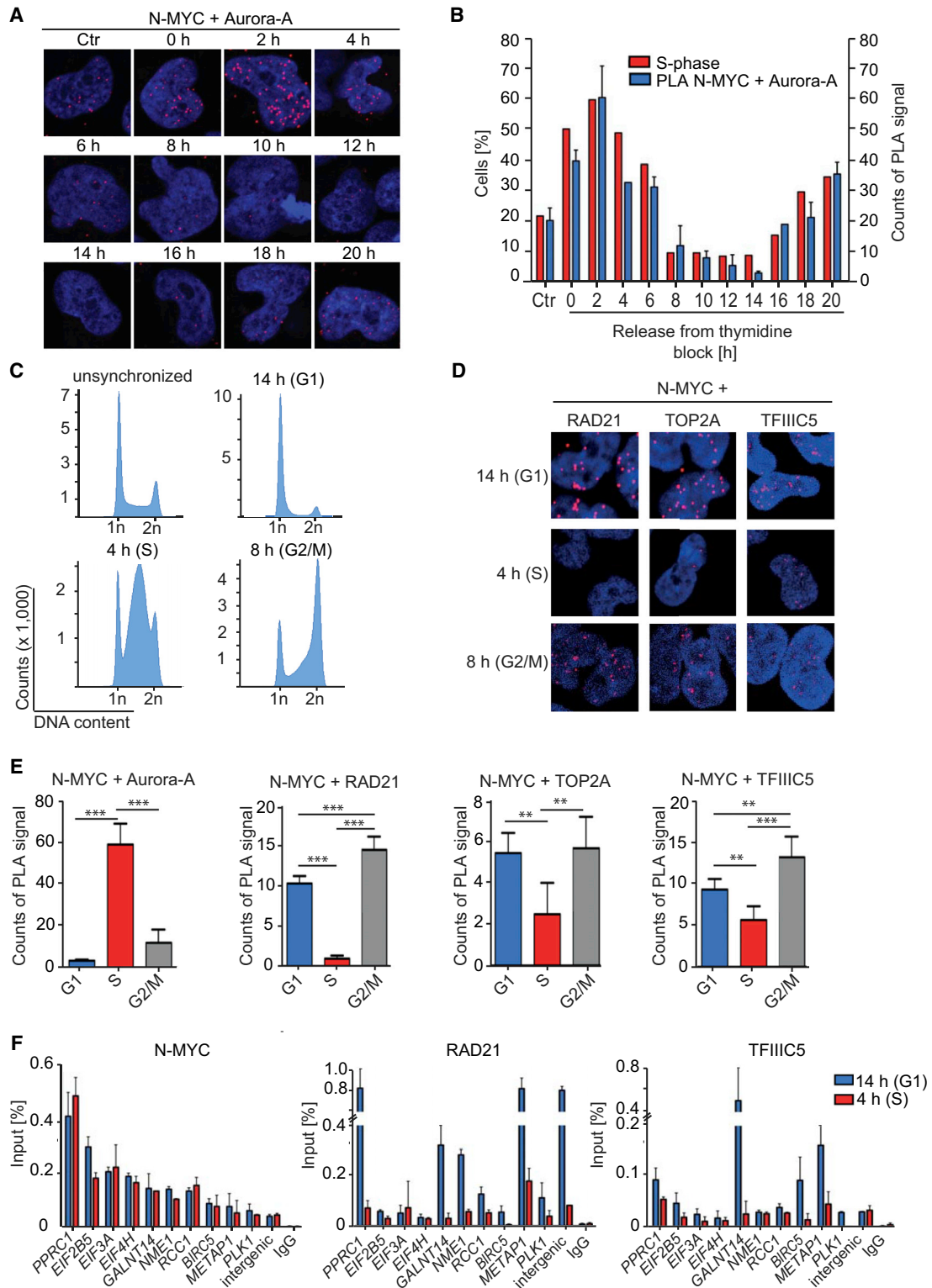See also Figure S3. n indicates the number of independent biological replicas for each experiment.

Figure 5. Regulation of N-MYC Transcription Complexes during the Cell Cycle

(A) Representative pictures from proximity ligation assays (PLAs) documenting complex formation between N-MYC and Aurora-A in IMR-5 cells after release from a double thymidine block. Non-synchronized cells are shown as a control (Ctr). Nuclei were stained using Hoechst. Red dots show PLA signals resulting from N-MYC/Aurora-A interactions (n = 3).

(legend continued on next page)

antibody in SH-EP cells that do not express N-MYC (Figure S5A) or using no primary antibody (Figure S5B) established that the signals observed in these assays are specific. We used either a release from a double thymidine block (Figure S5C) or re-stimulation of serum-starved cells (Figure S5D) to synchronize cells. In both experimental settings, Aurora-A predominantly associated with N-MYC during the S phase of the cell cycle, and complex formation was regulated independently of changes in overall N-MYC and Aurora-A protein levels (Figures 5A, 5B, and 5E; Figures S5E and S5F). We next tested whether association of N-MYC with cofactors changes throughout the cell cycle. Neither the association of N-MYC with p400 and TRRAP, which is mediated by MYCBoxII (amino acids 128–143), nor the interactions with the PAF1 components CTR9 and CDC73, for which the interaction domains are unknown, varied throughout the cell cycle (Figure S5G). In contrast, association of RAD21 with N-MYC was essentially absent during S phase (Figures 5C–5E). Similarly, associations of N-MYC with TOP2A and TFIIIC5 changed during cell cycle progression and were significantly lower in S phase (Figures 5C–5E; Figure S5H). ChIP experiments from cells harvested in G1 and S phase showed that association of N-MYC with joint binding sites was essentially equal in both cell cycle phases, whereas chromatin association of RAD21 was strongly reduced in S relative to G1 phase (Figure 5F). Chromatin association of TFIIIC was also reduced in S phase, but the extent of decrease was more variable between different gene loci. We concluded that complex formation of N-MYC with RAD21, TFIIIC, and TOP2A and chromatin binding of RAD21 and TFIIIC are reduced during S phase.

Aurora-A Antagonizes N-MYC/RAD21 Complex Formation in S Phase

We showed previously that association with N-MYC activates the catalytic activity of Aurora-A (Richards et al., 2016), and large-scale proteomic analyses show that multiple proteins associated with N-MYC, including TFIIIC2 and TOP2A, are phosphorylated in an Aurora-A-dependent manner *in vivo* (Kettenbach et al., 2011). These findings, and the observation that Aurora-A competes with association of RAD21 with N-MYC, led us to hypothesize that Aurora-A may antagonize complex formation of N-MYC with RAD21, TOP2A, and, potentially, TFIIIC during S phase. To test this, we used three structurally well-characterized Aurora-A inhibitors to acutely antagonize Aurora-A (Figure 6A; Richards et al., 2016). Of the inhibitors used, MK-5108 is a purely catalytic Aurora-A inhibitor that does not alter the conformation of Aurora-A and does not affect complex formation with N-MYC. MLN8237 inhibits both the catalytic

activity of Aurora-A and moderately distorts the N-MYC/Aurora-A complex, enhancing degradation of N-MYC by FBXW7 in mitosis. CD532 strongly distorts the Aurora-A structure, dissociates the N-MYC/Aurora-A complex, and induces subsequent degradation of Aurora-A and N-MYC (Richards et al., 2016). We confirmed that CD532 causes a proteasome-dependent decrease in N-MYC and Aurora-A levels (Figures S6A and S6B). In contrast, CD532 had no effect on complex formation of TFIIIC5 with RAD21 (Figure 3B).

PLA assays from cells released for 4 hr from a double thymidine block into S phase showed that MK-5108 and MLN8237 enhanced interactions of N-MYC with TFIIIC5, TOP2A, and, albeit more weakly, RAD21 (Figures 6B and 6C). In these assays, MK-5108 had the strongest effect. CD532 and MLN8237 had smaller and more variable effects in PLAs with TOP2A, RAD21, and TFIIIC5, most likely because the observed signals reflect a combination of the decrease in N-MYC levels and an increase in interaction (Figures 6A–6C). The data argue that Aurora-A-dependent phosphorylation antagonizes interactions of N-MYC with all three proteins.

ChIP and ChIP sequencing showed that chromatin association of N-MYC decreased in response to CD532, consistent with the effects on protein levels (Figures 6D and 6E; Figure S6C). In contrast, CD532 globally increased TFIIIC binding to chromatin (Figure 6D; Figure S6D), and the number of joint N-MYC/TFIIIC binding sites increased to 7,994 in the presence of CD532 (Figure S6E; note that N-MYC binding to chromatin remains detectable at virtually all sites after 4 hr of CD532 treatment). ChIP assays confirmed that CD532 enhanced stable chromatin binding of TFIIIC and RAD21 at joint binding sites, whereas the effects of MLN8237 and MK-5108 were weak for most sites (Figure 6E). We concluded that a decrease in Aurora-A levels or dissociation of N-MYC/Aurora-A complexes promotes stable association of TFIIIC and RAD21 with N-MYC-bound loci in S phase; it is also possible that inhibition of Aurora-A-dependent TFIIIC2 phosphorylation contributes to the increase. Notably, chromatin association of TFIIIC also increased in response to CD532 on sites where no N-MYC peak was detected in ChIP sequencing (Figure S6E). It is possible, therefore, that Aurora-A inhibits TFIIIC binding to chromatin also when complexed by other transcription factors. However, removing the inherent threshold in peak-calling algorithms revealed the presence of N-MYC at the majority (26,165 of 36,736) of all TFIIIC sites detectable after CD532 treatment (Figure S6F). Most likely, therefore, N-MYC is associated with the majority of all TFIIIC sites.

(B) Quantification of the PLA shown in (A). The percentage of cells in S phase is indicated in parallel. Error bars show SD of technical triplicates from one representative experiment (n = 3).

(C) Representative FACS profiles of propidium iodide (PI)-stained cells documenting cell cycle distribution at the indicated times after release from a double thymidine block.

(D) Representative pictures from PLAs documenting complex formation between N-MYC and RAD21 and TOP2A and TFIIIC5 in IMR-5 cells at the indicated times after release from a double thymidine block. Nuclei were stained using Hoechst. Red dots show PLA signals (n = 3).

(E) Quantification of PLAs shown in (A) and (D). Bars show mean + SD of technical triplicates from one representative experiment (n = 3). **p < 0.01, ***p < 0.001.

(F) ChIP of IMR-5 cells documenting chromatin association of N-MYC, RAD21, and TFIIIC5 at the indicated gene loci at the indicated times after release from a double thymidine block. Error bars show SD of technical triplicates from one representative experiment (n = 3).

See also Figure S5. n indicates the number of independent biological replicas for each experiment.
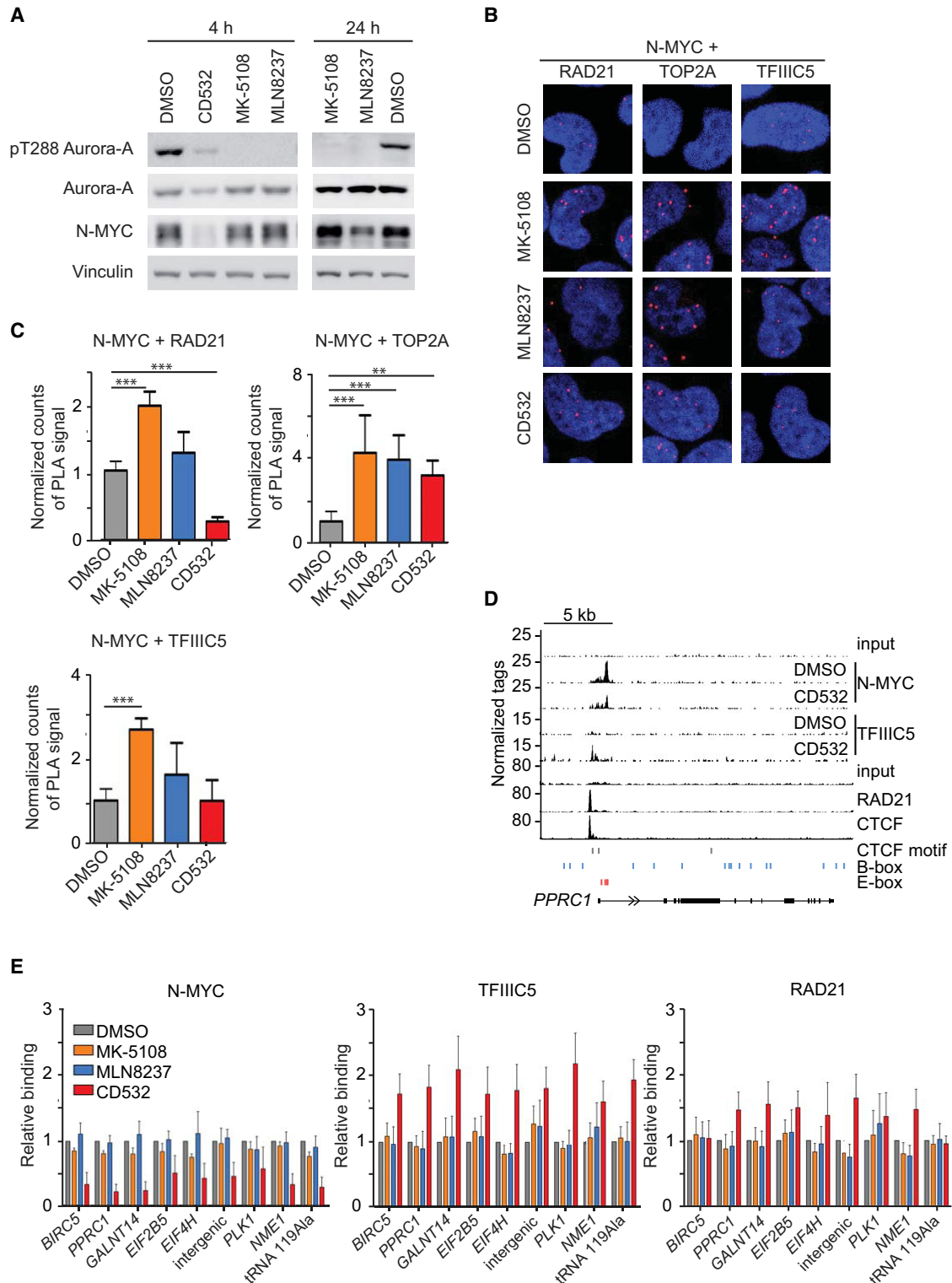
Figure 6. Role of Aurora-A in Dynamics of N-MYC Complexes during the Cell Cycle

(A) Immunoblot documenting levels of the indicated proteins and of Aurora-A, which is autophosphorylated at T288 (indicating catalytically active Aurora-A), in IMR-5 *MYCN*-amplified neuroblastoma cells after 4 hr (left) or 24 hr (right) exposure to 1 μM of the indicated Aurora-A inhibitors (n = 4).

(legend continued on next page)

Cell Cycle-Dependent Regulation of Pause Release by Aurora-A

To understand the role of TFIIIC in N-MYC-dependent pause release of Pol II, we analyzed SH-EP neuroblastoma cells, which express an N-MYCER chimeric protein that can be activated by addition of 4-Hydroxytamoxifen (4-OHT). We engineered these cells to express a doxycycline-inducible shRNA targeting TFIIIC5 (Figure 7A) and performed ChIP sequencing with antibodies directed against total Pol II before and 5 hr after addition of 4-OHT. Inspection of individual genes (*ODC1* and *NPM1*) (Figure S7A) and global analyses (Figures 7B and 7C; Figure S7B) showed that activation of N-MYC led to a strong decrease in Pol II occupancy at the transcription start site and a corresponding decrease in the Pol II "traveling ratio," which is defined as the ratio of Pol II occupancy at the promoter to occupancy in the gene body (Rahl et al., 2010). Depletion of TFIIIC5 by itself caused a moderate increase in Pol II promoter occupancy and Pol II traveling ratio (Figures 7B and 7C; Figures S7A and S7B). Intriguingly, depletion of TFIIIC5 abrogated the effect of N-MYCER on Pol II (Figures 7B and 7C; Figures S7A and S7B).

To understand which of N-MYC's effects on Pol II depend on TFIIIC, we performed ChIPs using antibodies that specifically recognize hypo-phosphorylated Pol II (8WG16) (Stock et al., 2007) or Pol II phosphorylated at Ser5, which occurs during escape of Pol II from the promoter, or at Ser2, which is a hallmark of pause release of Pol II, respectively. Intriguingly, ChIP sequencing showed that activation of N-MYC had no significant effect on chromatin association of hypo-phosphorylated Pol II (Figure S7C). To pinpoint the effect of N-MYC on Pol II function, we analyzed the association of Pol II with several MYC target genes for which Pol II does not decrease strongly at the promoter after N-MYC activation. Consistent with the ChIP sequencing data, neither activation of N-MYC nor depletion of TFIIIC5 had a significant effect on the association of hypo-phosphorylated Pol II with the transcription start site of several N-MYC target genes (Figure 7D). In contrast, depletion of TFIIIC5 abrogated both an N-MYC-dependent increase of Pol II that is phosphorylated at Ser5 at the transcription start site and of Pol II phosphorylated at Ser2 at the transcription end site (Figure 7D). Collectively, the data argue that TFIIIC5 is required for N-MYC-dependent escape of Pol II from the promoter and the subsequent pause release of Pol II.

To understand whether N-MYC-dependent pause release is cell cycle-regulated and whether Aurora-A affects this process, we activated N-MYCER in cells synchronized in S phase by a double thymidine block (Figures 7E and 7F). Under these circumstances, activation of N-MYC did not promote pause release of

Pol II; rather, activation of N-MYC caused a slight global increase in Pol II occupancy at core promoters, consistent with observations that MYC proteins can enhance promoter association of Pol II (Jaenicke et al., 2016). To test whether Aurora-A is required to block N-MYC-dependent pause release in S phase, we added CD532 to synchronized cells and performed ChIP sequencing both in the presence and absence of 4-OHT. Addition of CD532 to cells with activated N-MYC globally enhanced association of Pol II with the body of transcribed genes (Figure 7E; Figure S7D). In contrast, CD532 had little effect on Pol II function in cells with inactive N-MYCER, arguing that the effects on Pol II are mediated via N-MYC (Figure 7E; Figure S7D). CD532 also enhanced association of Pol II with the promoter in a N-MYC-dependent manner and, as consequence, did not alter the overall traveling ratio (Figure S7E). Furthermore, CD532 increased chromatin association of pSer2-Pol II in the gene body and at the transcription end site, and the effect was stronger in the presence of active N-MYC (Figure 7E). We concluded that association with Aurora-A antagonizes N-MYC-dependent promoter binding of Pol II and transcriptional elongation during S phase.

Finally, we explored a possible effect of enhanced transcriptional elongation on DNA replication and monitored phosphorylation of the single-strand DNA binding protein RPA32 at S33, which is phosphorylated by the ATR kinase in response to replication stress (Figure S7F; Liu et al., 2012). Inhibition of Aurora-A during the release of IMR-5 cells from a double thymidine block markedly enhanced phosphorylation of this site. In contrast, we did not observe phosphorylation of RPA32 at S4 and S8, target sites of DNA-dependent protein kinase (DNA-PK), and no activation of CHK1 and stabilization of p53 (Figure S7F). Consistently, inhibition of Aurora-A perturbed S phase progression, but did not prevent S phase entry or induce apoptosis (Figure S7G; Discussion). A model summarizing our findings is shown in Figure 7G.

DISCUSSION

We performed a proteomic analysis of N-MYC complexes in neuroblastoma cells and confirmed previously identified interactions of MYC and N-MYC proteins with MAX, the NuA4 complex, BPTF, p400, and the PAF1 complex. We also validated TFIIIC, RAD21, and TOP2A as interaction partners of N-MYC, arguing that N-MYC uses multiple effector proteins to regulate transcription. Previous proteomic analyses demonstrated the presence of TFIIIC and TOP2A in MYC complexes, suggesting that these interactions are conserved with MYC proteins (Koch et al., 2007).

Our data provide insights into how MYC accelerates several transitions of Pol II from one intermediate promoter state to the

(B) Representative pictures from PLAs documenting complex formation between N-MYC and RAD21 and TOP2A or TFIIIC5 in IMR-5 cells released for 4 hr from a double thymidine block in the presence of the indicated Aurora-A inhibitors (1 μM) or DMSO as a control. Nuclei were stained using Hoechst. Red dots show signals arising from interaction of N-MYC with the indicated proteins.

(C) Quantification of PLAs shown in (B). Data are normalized to DMSO-treated cells. Bars show mean + SD of technical triplicates from one experiment (n = 4). **p < 0.01, ***p < 0.001.

(D) Genome browser tracks at the *PPRC1* locus, illustrating chromatin association of the indicated proteins. The positions of B- and E-boxes and of CTCF motifs are indicated by vertical lines. The upper input is for ChIP sequencing of N-MYC and TFIIIC5, the lower input is for ChIP-sequencing of RAD21 and CTCF.

(E) ChIP of IMR-5 cells documenting chromatin association of N-MYC, TFIIIC5, and RAD21 at the indicated loci after treatment (1 μM) with MK-5108 (24 hr), MLN8237 (24 hr), CD532 (4 hr), or DMSO as a control. Error bars show SEM of three independent experiments. Data are normalized to DMSO-treated cells. See also Figure S6. n indicates the number of independent biological replicas for each experiment.
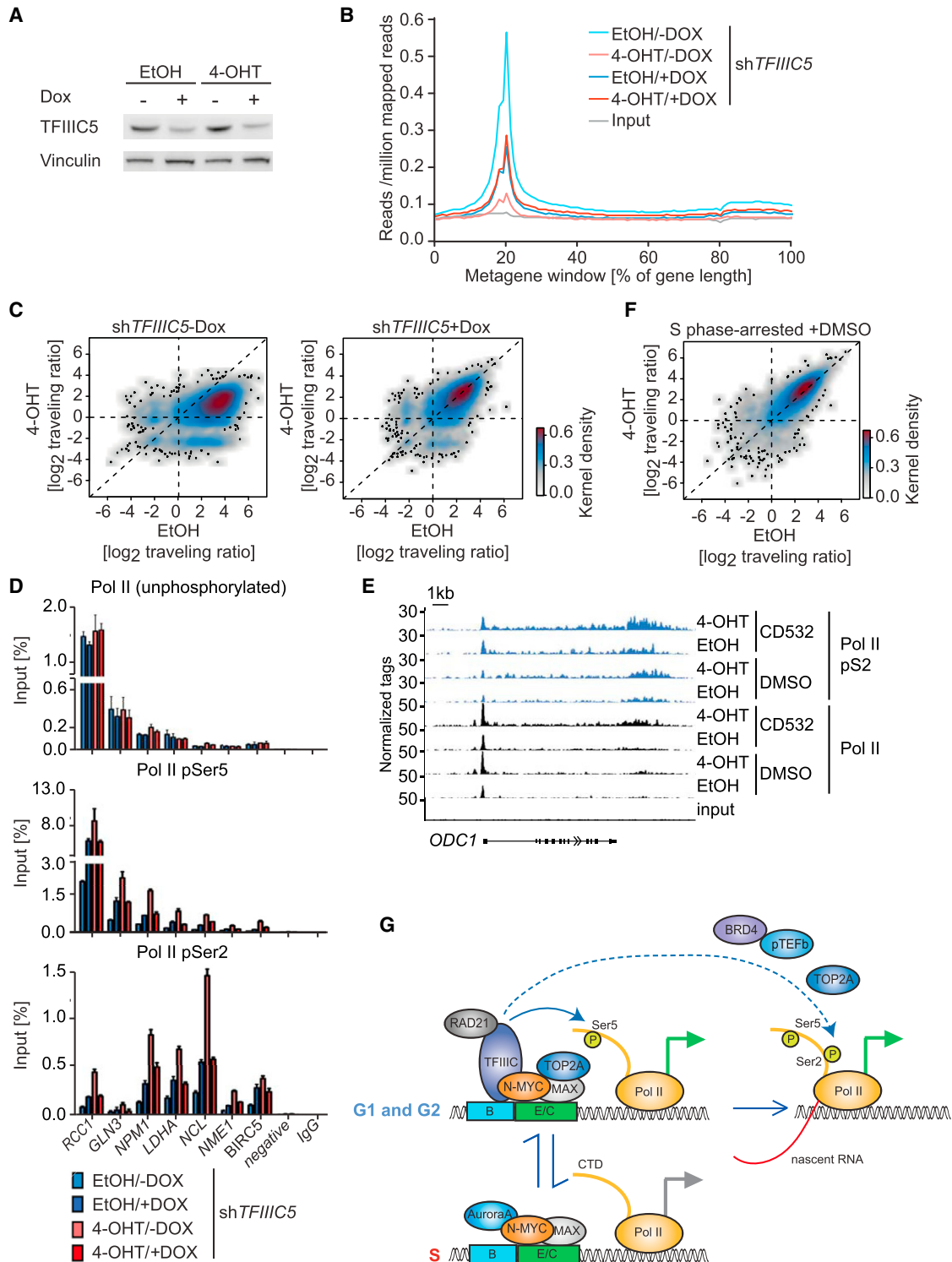
Figure 7. Aurora-A Suppresses N-MYC-Dependent Pause Release of Pol II in S phase

(A) Immunoblot showing levels of TFIIIC5 in SH-EP-N-MYCER cells expressing a Dox-inducible shRNA targeting TFIIIC5 (n = 3). Dox (1 μg ml^{-1}) was added for 30 hr; EtOH was used as a control.

(B) Metagene plot of all expressed genes (n = 14,650) illustrating distribution of Pol II within transcribed regions before and 5 hr after activation of N-MYCER in cells expressing Dox-inducible shTFIIIC5.

(legend continued on next page)

next. TFIIIC is both a general transcription factor of RNA polymerase III and an architectural protein (Van Bortle et al., 2014) and has been linked to the function of both cohesin and condensin complexes. In yeast, TFIIIC is required for loading condensin complexes onto tRNA genes (D'Ambrosio et al., 2008). In *Drosophila*, TFIIIC co-localizes with RAD21/cohesin at ETC sites (Van Bortle et al., 2014). Our ChIP sequencing data showed that N-MYC co-localizes with TFIIIC at multiple promoters and intergenic sites. TFIIIC is essential for transcription by RNA polymerase III, but the precise function of TFIIIC at ETC sites is unknown. We found that TFIIIC5 promotes association of RAD21 with N-MYC-bound promoters and is required for N-MYC-dependent phosphorylation of Pol II at Ser5 and Ser2 at several target genes, arguing that it promotes both promoter escape and pause release of Pol II. ChIP experiments suggest a hierarchy in which N-MYC promotes binding of TFIIIC, and TFIIIC, in turn, recruits RAD21. Because RAD21 and cohesin can promote pause release of Pol II (Schaaf et al., 2013), we suggest that N-MYC-dependent recruitment of RAD21 via TFIIIC facilitates promoter escape and pause release of Pol II in an enhancer-dependent manner. The model is consistent with the recent observation that depletion of RAD21 represses expression of N-MYC and MYC target genes (Rohban et al., 2017). Because the identity of active enhancers is characteristic for each cell, a model in which N-MYC facilitates the function of pre-existing enhancers could explain how N-MYC can "amplify" a pre-existing gene expression program.

Topoisomerase I is activated at core promoters via direct association with Pol II and promotes pause release because it relieves the torsional stress that builds up during early stages of transcription (Baranello et al., 2016). Because TOP2A associates with promoters of highly transcribed genes (Kouzine et al., 2013), it is likely that the association with N-MYC similarly relieves torsional stress during early stages of transcription, suggesting that multiple protein-protein interactions enable MYC proteins to facilitate consecutive steps of transcription (Figure 7G).

Unexpectedly, complexes of N-MYC are highly dynamic during the cell cycle. *In vitro*, Aurora-A competes with binding of TFIIIC and RAD21 to the amino-terminus of N-MYC. A secondary binding site for Aurora-A overlaps with MYCBoxIV, which binds to HCF1, and it is possible, therefore, that Aurora-A also competes with HCF1 for binding to N-MYC (Thomas et al., 2016). *In vivo*, Aurora-A inhibits chromatin binding of TFIIIC and RAD21 and interactions of N-MYC with RAD21, TOP2A, and

TFIIIC in S phase (Figure 7G). N-MYC-dependent pause release is inhibited in S phase, and inhibition of Aurora-A using CD532 partially restores elongation. Why might this regulation be important? Inhibition of Aurora-A during S phase activates the ATR kinase, which monitors replication stress (Hamperl and Cimprich, 2016). Phosphorylation of RPA32 at S33 with no CHK1 phosphorylation, as observed here, has been linked to recovery of collapsed replication forks rather than CHK1-mediated cell cycle arrest and DNA repair (Shiotani et al., 2013). We hypothesize, therefore, that MYC-dependent transcriptional elongation has an inherent potential to cause conflicts with DNA replication and that complex formation of N-MYC with Aurora-A is one of several co-transcriptional mechanisms that prevent such conflicts (Hamperl and Cimprich, 2016). Notably, TFIIIC binding was detected at many sites on chromatin at which we did not detect N-MYC, and TFIIIC binding was regulated by Aurora-A also at such sites. It is possible, therefore, that Aurora-A also regulates TFIIIC chromatin association independently of N-MYC. However, removing the inherent threshold in peak calling revealed the presence of N-MYC at the majority of all TFIIIC sites.

Inhibition of Aurora-A shows therapeutic efficacy in multiple MYC- and N-MYC-driven tumor models (Dardenne et al., 2016; Dauch et al., 2016). Similarly, deregulated expression of MYC and N-MYC activates ATR, and inhibition of ATR or CHK1 are being explored as possible therapeutic strategies for MYC- and N-MYC-driven tumors (Cole et al., 2011; Murga et al., 2011). Our findings suggest that MYC-driven tumors are particularly dependent on Aurora-A to avoid transcription/replication conflicts and open the possibility for rational development of therapies targeting these tumors.

EXPERIMENTAL PROCEDURES

Further details and an outline of the resources used in this work can be found in the Supplemental Experimental Procedures.

Cell Culture and Cell Cycle Synchronization
Neuroblastoma cell lines (IMR-5, IMR-32, and SH-EP) were grown in RPMI-1640 supplemented with 10% fetal calf serum and penicillin/streptomycin. For synchronization in S phase, cells were treated for 16 hr with 2 mM thymidine, released for 8 hr into normal medium, and then blocked again (2 mM, 16 hr). For release, cells were washed with PBS before fresh medium was added.

High-Throughput Sequencing
ChIP and ChIP sequencing were performed as described previously (Walz et al., 2014). RNA sequencing was performed as described previously

(C) 2D kernel density plot showing the ratio of Pol II occupancy at the promoter to occupancy in the gene body (traveling ratio) in cells treated as above for all expressed genes (n = 14,650) before and after 5 hr of N-MYCER-activation.

(D). ChIP of SH-EP N-MYCER cells documenting chromatin association of hypo-phosphorylated Pol II and Pol II phosphorylated at Ser5 (pSer5) or Ser2 (pSer2) at the indicated gene loci before and 5 hr after activation of N-MYCER. Occupancy at the transcription start site (TSS) was analyzed for hypo-phosphorylated Pol II and pSer5Pol II. Occupancy at the transcription end site (TES) was analyzed for pSer2Pol II. Dox (1 μg ml^{-1}) was added for 30 hr; EtOH was used as a control. Error bars show SD of technical triplicates from one representative experiment (n = 3).

(E) Genome browser tracks illustrating chromatin association of Pol II and Pol II pSer2 at the *ODC1* locus. ChIP sequencing was performed on cells synchronized in S phase by double thymidine blockade and treated for 2 hr with CD532 where indicated (1 μM).

(F) 2D kernel density plot showing the Pol II traveling ratio in response to N-MYCER activation in SH-EP cells that were synchronized in S phase by double thymidine block for all expressed genes (n = 14,650) before and after 4 hr of N-MYCER activation.

(G) Model summarizing our findings. We propose that the multiple protein-protein interactions of N-MYC promote sequential phosphorylation events of Pol II and both promotor escape and pause release. The dashed line indicates that effects on pause release and Ser2 phosphorylation could be secondary to changes in Ser5 phosphorylation. E/C indicates that the complex associates with sites on chromatin that contain either an E-box or a CTCF motif.

See also Figure S7. n indicates the number of independent biological replicas for each experiment.

([Jaenicke et al., 2016](#)) using an Illumina NextSeq 500. Preparations of samples, data quality assessment, filtering, and mapping are described in the [Supplemental Experimental Procedures](#).

In Situ PLA

The PLA was performed using the Duolink *In Situ* Kit (Sigma-Aldrich) according to the manufacturer's protocol. Pictures were taken with a confocal microscope (Nikon Ti-Eclipse) at 60× magnification. For quantification, the dots in not less than 300 cells were counted using ImageJ (Wayne Rasband, NIH). Antibodies are listed in the resource table in the [Supplemental Experimental Procedures](#).

Statistical Methods

Statistical significance between experimental groups was determined by Student's t test or, when means of three or more groups were compared, by one-way ANOVA. Data analysis was performed with Prism5.0 software (GraphPad). $p < 0.05$ was considered statistically significant.

DATA AND SOFTWARE AVAILABILITY

The accession number for the RNA and ChIP sequencing data reported in this paper is GEO: GSE78957.

SUPPLEMENTAL INFORMATION

Supplemental Information includes Supplemental Experimental Procedures, seven figures, and one table and can be found with this article online at https://doi.org/10.1016/j.celrep.2017.11.090.

AUTHOR CONTRIBUTIONS

G.B., A.C., K.-Y.M., I.R., E.L., O.S., J.H., S.H., J.K., E.P., C.K., and H.M.M. performed the experiments. A.B. and S.W. analyzed the high-throughput data. G.B., L.C., D.S.R., E.W., R.B., and M.E. devised and supervised the experiments; M.E. wrote the paper.

DECLARATION OF INTERESTS

The authors declare no competing interests.

REFERENCES

Baranello, L., Wojtowicz, D., Cui, K., Devaiah, B.N., Chung, H.J., Chan-Salis, K.Y., Guha, R., Wilson, K., Zhang, X., Zhang, H., et al. (2016). RNA polymerase II regulates topoisomerase 1 activity to favor efficient transcription. Cell *165*, 357–371.

Beltran, H. (2014). The N-MYC oncogene: maximizing its targets, regulation, and therapeutic potential. Mol. Cancer Res. *12*, 815–822.

Blackwell, T.K., Huang, J., Ma, A., Kretzner, L., Alt, F.W., Eisenman, R.N., and Weintraub, H. (1993). Binding of MYC proteins to canonical and noncanonical DNA sequences. Mol. Cell. Biol. *13*, 5216–5224.

Carrière, L., Graziani, S., Alibert, O., Ghavi-Helm, Y., Boussouar, F., Humbert-claude, H., Jounier, S., Aude, J.C., Keime, C., Murvai, J., et al. (2012). Genomic binding of Pol III transcription machinery and relationship with TFIIS transcription factor distribution in mouse embryonic stem cells. Nucleic Acids Res. *40*, 270–283.

Chesler, L., Schlieve, C., Goldenberg, D.D., Kenney, A., Kim, G., McMillan, A., Matthay, K.K., Rowitch, D., and Weiss, W.A. (2006). Inhibition of phosphatidy-linositol 3-kinase destabilizes MYCN protein and blocks malignant progression in neuroblastoma. Cancer Res. *66*, 8139–8146.

Cole, K.A., Huggins, J., Laquaglia, M., Hulderman, C.E., Russell, M.R., Bosse, K., Diskin, S.J., Attiyeh, E.F., Sennett, R., Norris, G., et al. (2011). RNAi screen of the protein kinome identifies checkpoint kinase 1 (CHK1) as a therapeutic target in neuroblastoma. Proc. Natl. Acad. Sci. USA *108*, 3336–3341.

Cowling, V.H., and Cole, M.D. (2007). The MYC transactivation domain promotes global phosphorylation of the RNA polymerase II carboxy-terminal domain independently of direct DNA binding. Mol. Cell. Biol. *27*, 2059–2073.

Cox, J., and Mann, M. (2008). MaxQuant enables high peptide identification rates, individualized P.P.B.-range mass accuracies and proteome-wide protein quantification. Nat. Biotechnol. *26*, 1367–1372.

Crepaldi, L., Policarpi, C., Coatti, A., Sherlock, W.T., Jongbloets, B.C., Down, T.A., and Riccio, A. (2013). Binding of TFIIIC to sine elements controls the relocation of activity-dependent neuronal genes to transcription factories. PLoS Genet. *9*, e1003699.

D'Ambrosio, C., Schmidt, C.K., Katou, Y., Kelly, G., Itoh, T., Shirahige, K., and Uhlmann, F. (2008). Identification of cis-acting sites for condensin loading onto budding yeast chromosomes. Genes Dev. *22*, 2215–2227.

Dang, C.V. (2012). MYC on the path to cancer. Cell *149*, 22–35.

Dardenne, E., Beltran, H., Benelli, M., Gayvert, K., Berger, A., Puca, L., Cyrta, J., Sboner, A., Noorzad, Z., MacDonald, T., et al. (2016). N-MYC induces an EZH2-mediated transcriptional program driving neuroendocrine prostate cancer. Cancer Cell *30*, 563–577.

Dauch, D., Rudalska, R., Cossa, G., Nault, J.C., Kang, T.W., Wuestefeld, T., Hohmeyer, A., Imbeaud, S., Yevsa, T., Hoenicke, L., et al. (2016). A MYC-aurora kinase A protein complex represents an actionable drug target in p53-altered liver cancer. Nat. Med. *22*, 744–753.

DuBois, S.G., Marachelian, A., Fox, E., Kudgus, R.A., Reid, J.M., Groshen, S., Malvar, J., Bagatell, R., Wagner, L., Maris, J.M., et al. (2016). Phase I study of the Aurora A kinase inhibitor alisertib in combination with irinotecan and temozolomide for patients with relapsed or refractory neuroblastoma: a NANT (new approaches to neuroblastoma therapy) trial. J. Clin. Oncol. *34*, 1368–1375.

Fuchs, M., Gerber, J., Drapkin, R., Sif, S., Ikura, T., Ogryzko, V., Lane, W.S., Nakatani, Y., and Livingston, D.M. (2001). The p400 complex is an essential E1A transformation target. Cell *106*, 297–307.

Ghirlando, R., and Felsenfeld, G. (2016). CTCF: making the right connections. Genes Dev. *30*, 881–891.

Gomez-Roman, N., Grandori, C., Eisenman, R.N., and White, R.J. (2003). Direct activation of RNA polymerase III transcription by c-MYC. Nature *421*, 290–294.

Hamperl, S., and Cimprich, K.A. (2016). Conflict resolution in the genome: how transcription and replication make it work. Cell *167*, 1455–1467.

Hart, T., Chandrashekhar, M., Aregger, M., Steinhart, Z., Brown, K.R., MacLeod, G., Mis, M., Zimmermann, M., Fradet-Turcotte, A., Sun, S., et al. (2015). High-resolution CRISPR screens reveal fitness genes and genotype-specific cancer liabilities. Cell *163*, 1515–1526.

Jaenicke, L.A., von Eyss, B., Carstensen, A., Wolf, E., Xu, W., Greifenberg, A.K., Geyer, M., Eilers, M., and Popov, N. (2016). Ubiquitin-dependent turnover of MYC antagonizes MYC/PAF1C complex accumulation to drive transcriptional elongation. Mol. Cell *61*, 54–67.

Jonkers, I., and Lis, J.T. (2015). Getting up to speed with transcription elongation by RNA polymerase II. Nat. Rev. Mol. Cell Biol. *16*, 167–177.

Kettenbach, A.N., Schweppe, D.K., Faherty, B.K., Pechenick, D., Pletnev, A.A., and Gerber, S.A. (2011). Quantitative phosphoproteomics identifies

substrates and functional modules of Aurora and Polo-like kinase activities in mitotic cells. Sci. Signal. *4*, rs5.

Koch, H.B., Zhang, R., Verdoodt, B., Bailey, A., Zhang, C.D., Yates, J.R., 3rd, Menssen, A., and Hermeking, H. (2007). Large-scale identification of c-MYC-associated proteins using a combined TAP/MudPIT approach. Cell Cycle *6*, 205–217.

Kouzine, F., Gupta, A., Baranello, L., Wojtowicz, D., Ben-Aissa, K., Liu, J., Przytycka, T.M., and Levens, D. (2013). Transcription-dependent dynamic supercoiling is a short-range genomic force. Nat. Struct. Mol. Biol. *20*, 396–403.

Lin, C.Y., Lovén, J., Rahl, P.B., Paranal, R.M., Burge, C.B., Bradner, J.E., Lee, T.I., and Young, R.A. (2012). Transcriptional amplification in tumor cells with elevated c-MYC. Cell *151*, 56–67.

Liu, S., Opiyo, S.O., Manthey, K., Glanzer, J.G., Ashley, A.K., Amerin, C., Troksa, K., Shrivastav, M., Nickoloff, J.A., and Oakley, G.G. (2012). Distinct roles for DNA-PK, ATM and ATR in RPA phosphorylation and checkpoint activation in response to replication stress. Nucleic Acids Res. *40*, 10780–10794.

Marumoto, T., Zhang, D., and Saya, H. (2005). Aurora-A - a guardian of poles. Nat. Rev. Cancer *5*, 42–50.

McMahon, S.B., Van Buskirk, H.A., Dugan, K.A., Copeland, T.D., and Cole, M.D. (1998). The novel ATM-related protein TRRAP is an essential cofactor for the c-MYC and E2F oncoproteins. Cell *94*, 363–374.

Michel, M., and Cramer, P. (2013). Transitions for regulating early transcription. Cell *153*, 943–944.

Molenaar, J.J., Koster, J., Zwijnenburg, D.A., van Sluis, P., Valentijn, L.J., van der Ploeg, I., Hamdi, M., van Nes, J., Westerman, B.A., van Arkel, J., et al. (2012). Sequencing of neuroblastoma identifies chromothripsis and defects in neuritogenesis genes. Nature *483*, 589–593.

Moqtaderi, Z., Wang, J., Raha, D., White, R.J., Snyder, M., Weng, Z., and Struhl, K. (2010). Genomic binding profiles of functionally distinct RNA polymerase III transcription complexes in human cells. Nat. Struct. Mol. Biol. *17*, 635–640.

Murga, M., Campaner, S., Lopez-Contreras, A.J., Toledo, L.I., Soria, R., Montaña, M.F., Artista, L., Schleker, T., Guerra, C., Garcia, E., et al. (2011). Exploiting oncogene-induced replicative stress for the selective killing of Myc-driven tumors. Nat. Struct. Mol. Biol. *18*, 1331–1335.

Nie, Z., Hu, G., Wei, G., Cui, K., Yamane, A., Resch, W., Wang, R., Green, D.R., Tessarollo, L., Casellas, R., et al. (2012). c-MYC is a universal amplifier of expressed genes in lymphocytes and embryonic stem cells. Cell *151*, 68–79.

Oler, A.J., Alla, R.K., Roberts, D.N., Wong, A., Hollenhorst, P.C., Chandler, K.J., Cassiday, P.A., Nelson, C.A., Hagedorn, C.H., Graves, B.J., and Cairns, B.R. (2010). Human RNA polymerase III transcriptomes and relationships to Pol II promoter chromatin and enhancer-binding factors. Nat. Struct. Mol. Biol. *17*, 620–628.

Otto, T., Horn, S., Brockmann, M., Eilers, U., Schüttrumpf, L., Popov, N., Kenney, A.M., Schulte, J.H., Beijersbergen, R., Christiansen, H., et al. (2009). Stabilization of N-MYC is a critical function of Aurora-A in human neuroblastoma. Cancer Cell *15*, 67–78.

Rahl, P.B., Lin, C.Y., Seila, A.C., Flynn, R.A., McCuine, S., Burge, C.B., Sharp, P.A., and Young, R.A. (2010). c-MYC regulates transcriptional pause release. Cell *141*, 432–445.

Richards, M.W., Burgess, S.G., Poon, E., Carstensen, A., Eilers, M., Chesler, L., and Bayliss, R. (2016). Structural basis of N-MYC binding by Aurora-A and its destabilization by kinase inhibitors. Proc. Natl. Acad. Sci. USA *113*, 13726–13731.

Richart, L., Carrillo-de Santa Pau, E., Río-Machín, A., de Andrés, M.P., Cigudosa, J.C., Lobo, V.J., and Real, F.X. (2016). BPTF is required for c-MYC transcriptional activity and in vivo tumorigenesis. Nat. Commun. *7*, 10153.

Rohban, S., Cerutti, A., Morelli, M.J., d'Adda di Fagagna, F., and Campaner, S. (2017). The cohesin complex prevents MYC-induced replication stress. Cell Death Dis. *8*, e2956.

Sabò, A., Kress, T.R., Pelizzola, M., de Pretis, S., Gorski, M.M., Tesi, A., Morelli, M.J., Bora, P., Doni, M., Verrecchia, A., et al. (2014). Selective transcriptional regulation by MYC in cellular growth control and lymphomagenesis. Nature *511*, 488–492.

Schaaf, C.A., Kwak, H., Koenig, A., Misulovin, Z., Gohara, D.W., Watson, A., Zhou, Y., Lis, J.T., and Dorsett, D. (2013). Genome-wide control of RNA polymerase II activity by cohesin. PLoS Genet. *9*, e1003382.

Shen, Y., Igo, M., Yalamanchili, P., Berk, A.J., and Dasgupta, A. (1996). DNA binding domain and subunit interactions of transcription factor IIIC revealed by dissection with poliovirus 3C protease. Mol. Cell. Biol. *16*, 4163–4171.

Shiotani, B., Nguyen, H.D., Håkansson, P., Maréchal, A., Tse, A., Tahara, H., and Zou, L. (2013). Two distinct modes of ATR activation orchestrated by Rad17 and Nbs1. Cell Rep. *3*, 1651–1662.

Sjostrom, S.K., Finn, G., Hahn, W.C., Rowitch, D.H., and Kenney, A.M. (2005). The Cdk1 complex plays a prime role in regulating N-MYC phosphorylation and turnover in neural precursors. Dev. Cell *9*, 327–338.

Söderberg, O., Gullberg, M., Jarvius, M., Ridderstråle, K., Leuchowius, K.J., Jarvius, J., Wester, K., Hydbring, P., Bahram, F., Larsson, L.G., and Landegren, U. (2006). Direct observation of individual endogenous protein complexes in situ by proximity ligation. Nat. Methods *3*, 995–1000.

Stock, J.K., Giadrossi, S., Casanova, M., Brookes, E., Vidal, M., Koseki, H., Brockdorff, N., Fisher, A.G., and Pombo, A. (2007). Ring1-mediated ubiquitination of H2A restrains poised RNA polymerase II at bivalent genes in mouse ES cells. Nat. Cell Biol. *9*, 1428–1435.

Subramanian, A., Tamayo, P., Mootha, V.K., Mukherjee, S., Ebert, B.L., Gillette, M.A., Paulovich, A., Pomeroy, S.L., Golub, T.R., Lander, E.S., and Mesirov, J.P. (2005). Gene set enrichment analysis: a knowledge-based approach for interpreting genome-wide expression profiles. Proc. Natl. Acad. Sci. USA *102*, 15545–15550.

Thomas, L.R., Foshage, A.M., Weissmiller, A.M., Popay, T.M., Grieb, B.C., Qualls, S.J., Ng, V., Carboneau, B., Lorey, S., Eischen, C.M., and Tansey, W.P. (2016). Interaction of MYC with host cell factor-1 is mediated by the evolutionarily conserved MYC box IV motif. Oncogene *35*, 3613–3618.

Valentijn, L.J., Koster, J., Haneveld, F., Aissa, R.A., van Sluis, P., Broekmans, M.E., Molenaar, J.J., van Nes, J., and Versteeg, R. (2012). Functional MYCN signature predicts outcome of neuroblastoma irrespective of MYCN amplification. Proc. Natl. Acad. Sci. USA *109*, 19190–19195.

Van Bortle, K., Nichols, M.H., Li, L., Ong, C.T., Takenaka, N., Qin, Z.S., and Corces, V.G. (2014). Insulator function and topological domain border strength scale with architectural protein occupancy. Genome Biol. *15*, R82.

Vietri Rudan, M., and Hadjur, S. (2015). Genetic tailors: CTCF and cohesin shape the genome during evolution. Trends Genet. *31*, 651–660.

Walz, S., Lorenzin, F., Morton, J., Wiese, K.E., von Eyss, B., Herold, S., Rycak, L., Dumay-Odelot, H., Karim, S., Bartkuhn, M., et al. (2014). Activation and repression by oncogenic MYC shape tumour-specific gene expression profiles. Nature *511*, 483–487.

Welcker, M., Orian, A., Jin, J., Grim, J.E., Harper, J.W., Eisenman, R.N., and Clurman, B.E. (2004). The Fbw7 tumor suppressor regulates glycogen synthase kinase 3 phosphorylation-dependent c-MYC protein degradation. Proc. Natl. Acad. Sci. USA *101*, 9085–9090.

Supplemental Information

Association with Aurora-A Controls N-MYC-Dependent

Promoter Escape and Pause Release

of RNA Polymerase II during the Cell Cycle

Gabriele Büchel, Anne Carstensen, Ka-Yan Mak, Isabelle Roeschert, Eoin Leen, Olga Sumara, Julia Hofstetter, Steffi Herold, Jacqueline Kalb, Apoorva Baluapuri, Evon Poon, Colin Kwok, Louis Chesler, Hans Michael Maric, David S. Rickman, Elmar Wolf, Richard Bayliss, Susanne Walz, and Martin Eilers

Supplemental Experimental Procedures

CONTACT FOR REAGENT AND RESOURCE SHARING

Further information and requests for resources and reagents should be directed to and will be fulfilled by the Lead Contact, Martin Eilers (martin.eilers@biozentrum.uni-wuerzburg.de).

EXPERIMENTAL MODEL AND SUBJECT DETAILS

Cell culture

Neuroblastoma cell lines (IMR-5, IMR-32, SH-EP) were verified by STR profiling and grown in RPMI-1640 (Sigma-Aldrich and Thermo Fisher Scientific); HEK293TN and PlatE cells were grown in DMEM (Sigma-Aldrich and Thermo Fisher Scientific). Media were supplemented with 10% fetal calf serum (Biochrom) and penicillin/streptomycin (Sigma-Aldrich). All cells were routinely tested for mycoplasma contamination. For starvation experiments, IMR-5 cells were cultivated in serum-free medium for 48 h and then re-stimulated by change to media containing 10% fetal calf serum.

METHOD DETAILS

Transfection and lentiviral infection

For lentivirus production, HEK293TN cells were transfected using PEI (Polyethyleneimine, Sigma-Aldrich). Transfections of siRNAs were performed using RNAiMAX reagent and OptiMEM (Life Technologies) according to manufacturer's protocol. siRNAs used are listed in reference table. Cells were harvested 48 h after transfection. For production of stable SH-EP cell lines, PlatE cells were transfected with amino-terminal HA-tagged N-MYC expression plasmids. Retroviral supernatants were used for infection of SH-EP cells stably expressing the murine ecotropic receptor in the presence of 4 µg ml^{-1} polybrene (Sigma-Aldrich) for 24 h. Infected cells were selected with 3 µg ml^{-1} blasticidin for 2 weeks, clones were picked and expanded. Lentiviruses expressing a shRNA targeting TFIIIC5 (targeting sequence: AAGCGCAGCACCTACAACTACA), TFIIIC2 (targeting sequence:

TCCGTAGAGATGTCATTACCTA) or N-MYC (targeting sequence: GAGGAGCATGTTTTGTATACAA) were produced by transfection of pINDUCER-11 plasmid together with the packaging plasmid psPAX.2, and the envelope plasmid pMD2.G into HEK293TN cells. Virus-containing supernatant was harvested 24 h and 48 h after transfection. IMR-5 cells were infected with lentiviral supernatants in the presence of 4 µg ml^{-1} polybrene (Sigma-Aldrich) for 24 h. shRNA expression was stimulated by addition of doxycycline (1 µg ml^{-1}) for 12 h and cells were FACS-sorted for RFP-positive cells. Cells were harvested 48 h after induction with doxycycline (1 µg ml^{-1}) or ethanol as control.

For CRISPR-constructs guide-RNA (gRNA) were designed based on target sequences against TFIIIC5 reported in Hart et al. (Hart et al., 2015). Oligonucleotides were annealed and cloned into the BsmBI-BsmBI sites downstream from the human U6 promoter in the lentiCRISPR v2 plasmid. Lentivirus production and infection was done as described above. Cells were treated with 0.05 µg ml^{-1} of puromycin to select resistant cells.

Sequences of gRNA.

	Gene specific part TFIIIC5-exons
TFIIIC5-gRNA-1	CCCTGCCAGACGCACAGGGA
TFIIIC5-gRNA-2	GCTCATGCTCCGGCCCGAGA
TFIIIC5-gRNA-3	GAATCCATAGGCTGCGCCAG
TFIIIC5-gRNA-5	CATTTCGGGACCAGATGGGA
TFIIIC5-gRNA-6	GAGAACGAGGCGGCAGAAAG
TFIIIC5-gRNA-7	ATGGTGTGCGTGGAGTACCC
TFIIIC5-gRNA-8	ACCGACCAGAGACCCAGCAC

Clonogenic assay

IMR-5 and SH-EP cells expressing a doxycycline-inducible shRNA targeting shTFIIIC5 were seeded at low density and treated with doxycycline or ethanol as control until cells were confluent. Cells were fixed by adding 3.7% formaldehyde to the medium for 15 min. After removing the medium dishes were dried over night. 2 ml of 0.1% crystal violet staining solution was added and incubated for 2 h at room temperature. Dishes were washed in a stream of tap water. After washing dishes were inverted and dried over night.

Immunoblots and immunoprecipitations

Whole-cell extracts were prepared using NP-40 buffer (50 mM Tris (pH 8.0), 150 mM NaCl, 1% NP-40, and a cocktail of protease inhibitors) with three rounds of freeze/thaw cycles or RIPA buffer (50 mM HEPES, 140 mM NaCl, 1 mM EDTA; 1% Triton X-100, 0,1% Nadeoxycholate, 0,1% SDS) containing protease and phosphatase inhibitor cocktails (Sigma-Aldrich). Lysates were cleared by centrifugation, separated on SDS or Bis-Tris gels and transferred to a PVDF membrane (Millipore). Antibodies are listed in the resource table.

For immunoprecipitation, cells were re-suspended in lysis buffer containing 20 mM HEPES-KOH (pH 7.8), 140 mM KCl, 0.2 mM EDTA, 0.1% NP-40 supplemented with a cocktail of protease and phosphatase inhibitors. After brief sonication, samples were incubated on ice for 30 min and cleared by centrifugation. Co-immunoprecipitation was carried out in lysis buffer using 2 µg of antibodies and 1–2 mg lysate.

Flow cytometry analysis (FACS)

BrdU-PI-FACS was performed as described previously (Schulein-Volk et al., 2014). Subconfluent cells were labelled with 20 µM 5-Bromo-2'-deoxyuridine (BrdU, Sigma-Aldrich) for 1 h. Cells were harvested together with the supernatant, washed with ice-cold PBS and fixed in 80% ethanol overnight at -20 °C. Cells were washed with cold PBS and incubated in 2 M HCl/0.5% Triton X-100 for 30 minutes at room temperature. Cell pellets were neutralized by incubating with $Na_2B_4O_7$. The pellet was incubated with Anti-BrdU-FITC antibody diluted in 100 µl 1 % BSA, 0.5 % Tween-20 in PBS for 30 minutes at room temperature in the dark. After washing with PBS, the cells were re-suspended in PBS with RNAse A (24 µg ml^{-1}) and propidium iodide (PI, 54 µM) and incubated for 30 min at 37 °C.

For PI-FACS cells were harvested by trypsinization, washed with cold PBS and fixed in 80% ethanol overnight at −20 °C. After washing with PBS, the cells were re-suspended in PBS with RNAse A (24 µg ml^{-1}) and PI (54 µM) and incubated for 30 min at 37 °C. Subsequent analysis was performed on a BD FACSCanto II flow cytometer using BD FACSDIVA^{TM} Software.

Mass spectrometric analysis

Proteins from immunoprecipitations were dissolved in NuPAGE LDS sample buffer (Life Technologies), reduced with 50 mM DTT at 70 °C for 10 min, alkylated with 120 mM iodoacetamide at room temperature for 20 min and separated on NuPAGE Novex 4-12% Bis-Tris gels (Life Technologies) with MOPS buffer according to manufacturer's instructions. Gels were stained for 45 min with Simply Blue™ Safe Stain (Life Technologies). Each gel lane was cut into 15 bands, gel bands were chopped and destained with 70% acetonitrile in 100 mM NH_4HCO_3 (pH 8), shrunk with 100% acetonitrile and dried in a vacuum concentrator (Concentrator 5301, Eppendorf). Dried gel pieces were suspended in 100 mM NH_4HCO_3 (pH 8) containing 0.1 µg trypsin (Trypsin Gold, Mass Spectrometry Grade, Promega) and proteins were digested overnight at 37 °C.

NanoLC-MS/MS analyses were performed on an LTQ-Orbitrap Velos Pro (Thermo Scientific) equipped with an EASY-Spray Ion Source and coupled to an EASY-nLC 1000 (Thermo Scientific). Peptides were loaded on a trapping column (2 cm x 75 µm ID. PepMap C18 3 µm particles, 100 Å pore size) and separated on an EASY-Spray column (25 cm x 75 µm ID, PepMap C18 2 µm particles, 100 Å pore size) with a 30-minute linear gradient from 3% to 30% acetonitrile and 0.1% formic acid. MS scans were acquired in the Orbitrap analyser with a resolution of 30,000 at m/z 400, MS/MS scans were acquired in the Orbitrap analyser with a resolution of 7,500 at m/z 400 using HCD fragmentation with 30% normalized collision energy. A TOP5 data-dependent MS/MS method was used. Lock mass option was applied for internal calibration in all runs using background ions from protonated decamethylcyclopentasiloxane (m/z 371.10124).

Mascot Distiller 2.4 (Matrix Science) was used for raw data processing and for generating peak lists with standard settings for the Orbitrap Velos. Mascot Server 2.4 was used for database searching with the following parameters: peptide mass tolerance: 8 ppm, MS/MS mass tolerance: 0.02 Da, enzyme: "trypsin" with three missed cleavage sites allowed for trypsin, fixed modification: carbamidomethyl (C), variable modifications: Gln->pyroGlu (N-term. Q) and oxidation (M). Database searching was performed against UniProt human

database. Spotfire was used to visualize data. Protein scores were calculated using MaxQuant (Cox and Mann, 2008).

In vitro binding assays

Constructs encoding FLAG-tagged fragments of the N-MYC transactivation domain were cloned into pETM6T1 and expressed as His-NusA fusions. These were purified on 5 ml chelating Sepharose columns (GE Healthcare) charged with nickel; the His-NusA tags were cleaved away using TEV NIa protease and removed by nickel affinity chromatography and the FLAG-N-MYC fragments were further purified by gel filtration using a Superdex 75 column (GE Healthcare) into N-MYC fragment buffer (20 mM HEPES pH 7.5, 100 mM NaCl). For *in vitro* pull-down assays from HeLa cell lysate, recombinant N-MYC fragments were immobilised on 30 µl Anti-FLAG M2 affinity gel (Sigma-Aldrich) and incubated with 1.2 mg of HeLa cell lysate in 150 mM sodium chloride, 50 mM Tris pH 8.0, 1.0% NP-40 and 1x Roche complete protease inhibitors. The final volume of the mix was made up to 495 µl with N-MYC fragment buffer. The concentration of FLAG-N-MYC fragments was determined by absorbance at 280 nm, however adjustments were made to account for differences observed in apparent concentration by immunoblots. The final protein concentrations were 9.3 µM for all fragments apart from N-MYC 1-137 (6.2 µM) and 46-89 (14.3 µM). The mixture was incubated by slow rotation at 4 °C for two hours prior to washing the gel three times with 500 µl N-MYC fragment buffer. FLAG-tagged fragments were eluted by addition of 85 µl of N-MYC fragment buffer with 0.25 mg ml^{-1} 3x FLAG-peptide (Sigma-Aldrich). This mix was allowed to rotate at 4 °C for 30 minutes prior to collection of eluates. Mixes and eluate fractions were subjected to SDS-PAGE and subsequently analyzed by immunoblotting. The competition assays were performed as described above with the exception that mixtures were spiked with either recombinant Aurora-A kinase or an equivalent amount of Aurora-kinase buffer. The recombinant Aurora-A protein used comprised residues 122-403 and C290A:C393A (Burgess and Bayliss, 2015). Expression and purification was performed as previously described (Bayliss et al., 2003). The protein was finally buffer exchanged by

repeated dilution and concentration into 150 mM NaCl, 20 mM HEPES pH 7.5, 5 mM MgCl$_2$, and 10% glycerol.

High-throughput sequencing

ChIP and ChIP-sequencing was performed as described previously (Walz et al., 2014). Cells were treated with 1% formaldehyde for 10 min at room temperature following 5 min of incubation with glycine. After cell lysis (5 mM PIPES pH 8.8, 5 mM KCl, 0.5% NP40), nuclei were re-suspended in RIPA buffer (50 mM HEPES pH 7.9, 140 mM NaCl, 1% Triton-X-100, 0.1% deoxycholic acid (DOC), 0.1% SDS, 1 mM EDTA containing protease inhibitor cocktail) and DNA was fragmented to a size <500 bp using a Branson sonifier. Antibodies were bound to Protein A/G-dynabeads (Invitrogen) and immunoprecipitated. Chromatin was eluted with 1% SDS and crosslinking was reverted overnight. Chloroform/phenol extraction was used for purification. ChIP-sequencing was performed as described before (Chen et al., 2008). Purified DNA was end-repaired, A-tailed, ligated to Illumina adaptors, size-selected (200 bp) and purified with Qiagen gel extraction kit. DNA fragments were amplified by 15-18 cycles of PCR and library size was tested with the Biorad Experion system. The amount of library DNA was quantified using a picogreen assay and subjected to Illumina GAIIx or Illumina NextSeq 500 sequencing according to the manufacturer's instructions. After base calling with the Genome Analyzer Data Collection Software, high quality PF-clusters (according to the CASAVA filter) were selected for further analyses. Antibodies are listed in the resource table. All ChIP-sequencing experiments were performed 1-3 times and results validated with independent ChIPs on individual genes.

Sequences of oligonucleotides for qPCR.

	forward	reverse
BIRC5 TSS	CTTTGAAAGCAGTCGAGGGG	TGTGCCGGGAGTTGTAGTC
BIRC5 TES	GGTCTGTGTTGAGAGGGTGA	GAAGTCAAGGCCCCAGTTTG
CDK14	CCCTCTCCTTCAATCCATCA	CGGAGCAGCAGAATCTGTAGT
CLINT1	GGCACTCTCAACGGTTTCTT	AAATTTATTGGGGAGGGGCG
EIF2B5	TTTTCGTTCCGCACCCTAAC	CTGAGAGCTGTTTCCACGTG
EIF3A	GAGAGGAGACGAAGGGGAAC	GCTCCTTCCTTTCCGTCTCT
EIF4H	CAGCTCTCCAGGTCACCTC	CTACGCGGCCCATTATGTG
ERCC	CCTCACTATCATCCATCCGCT	AGGTTTCCCAGGCCTACTC

GALNT14 (N-MYC binding)	AATGTGCTCGTCCTACCACA	AGTAGCCAGGCAAGTGAACC
GALNT14	CTAGACCCAGGATCCGGTTG	CAGGCTCGCTTCTCTTCGA
GLN3 TSS	GTGACGCTCGTCAGTGG	CATATTGGCTGTAGAAGGAAGC
GLN3 TES	GTTATGGTATGCATGAGCTGTG	CTACTTCCACTCACAATGAGATG
Intergenic region (chr3)	TATGTTGCTGTCCACCCCAT	TATCTGTGTAGGCCAGGCTG
Intergenic region (chr5)	GAGGCCAGTGGAAAGAGACA	TCTTTAACCCACTGCCACCT
Intergenic region (chr6)	GGGCTGGATATGCAGTGGTA	CCTCTTTCCTTGTATATGGCTCC
Intergenic region (chr14)	CCTTCTCCTCCTTCAGCTCC	CTCTCTGGCCTGTTTCCTCA
Intergenic region (chr16)	GGAAGACACCTGTTGCCAAG	TCACAGGCAGATGGTTAGGC
Intergenic region (chr21)	CTTTCCCAGGGCGCCATC	GGCATCCCCGAGTCAGAC
Intergenic region	CACACGAGGGTCCATAACGT	GTGGATTTCAGAGCCATCCG
LDHA TSS	GGAGGGCAGCACCTTACTTA	GTGGAACAGCTATGCTGACG
LDHA TES	TGTGGAATCTTTTGCTTTCCCT	TGTTGGCCATGCTAGTCTTG
LHFPL	GCCATGCCTCAGTATCTCCT	GAACTTCAGTATCGGCCACC
MEI4	GCCATGCCTCAGTATCTCCT	TAAGACCCAACCGCCAGTAG
METAP1	AGGGAGGGCAGATGTGAATC	TCTTCACTGACGAACACCCA
Negative region (chr1)	GCAGTTCAACCTACAAGCCAATAGAC	CACAAATTAGCGCATTGCCTGA
Negative region (chr11)	TTTTCTCACATTGCCCCTGT	TCAATGCTGTACCAGGCAAA
NCL TSS	CTACCACCCTCATCTGAATCC	TTGTCTCGCTGGGAAAGG
NCL TES	AGCCTTCATCCAGGTGAGAA	GGCCACACGGCATATAGACT
NME1 TSS	GGGGTGGAGAGAAGAAAGCA	TGGGAGTAGGCAGTCATTCT
NME1 TES	GATTGCTGAGGTGCTTGGAG	AGCAACTCAAGAGGCTGAGT
NPM1 TSS	TTCACCGGGAAGCATGG	CACGCGAGGTAAGTCTACG
NPM1 TES	TAGGGCGTGGGTCTTTTCTT	AACTTGGGACCTCTACTGCC
PLK1	GTTTGAATTCGGGGAGGAGC	CAGTCACTGCAGCACTCATG
PPRC1 (N-MYC binding	GAAGGCTGAGACCTCCATGT	GTTCTCCCGGGAAAATTGCT
PPRC1	GTGAGGATTAGCGCTTGGAG	TGCTGACGTTCCTTTCACC
RCC1 TSS (N-MYC binding	AGTGGTCGCTTCTTCTCCTT	GCATTAGACCCACAACTCCG
RCC1 TSS	GTAGCTGGGACTGGAGGTG	TTGAGGCCAGGAGTTCGAG
RCC1 TES	TGTGGTATGGGACTGTGCAA	ACTCCTGACCTCAAGCGATC
tRNA119Ala	ACTTGTGCCAGGGGATGTAG	AATCTACGTGATCGCCTTGG
tRNA7Leu	ATGTAGCATAAGCGCGTCAG	ACTGTCAGGAGTGGGATTCG

RNA-sequencing was performed as described previously (Jaenicke et al., 2016) using an Illumina NextSeq 500. RNA was extracted using RNeasy mini columns (Qiagen) including on-column DNase I digestion. mRNA was isolated using the NEBNext® Poly(A) mRNA Magnetic Isolation Module (NEB) library preparation was performed with the NEBNext®

Ultra™ RNA Library Prep Kit for Illumina following the instruction manual. Libraries were size-selected using Agencourt AMPure XP Beads (Beckman Coulter) followed by amplification with 12 PCR cycles. Library quantification and size determination was performed with the Experion Automated Electrophoresis System (Bio-Rad).

Peptide microarrays

For evaluation in microarray format Myc peptides were synthesized in parallel using a ResPep SL synthesis robot (Intavis AG) equipped with a Celluspot synthesis module and printed using a slide spotting robot (Intavis AG). Total synthesis time was 256 h. Coupling reagents were freshly prepared every 48 h. Synthesis was based on Standard Fluorenylmethoxycarbonyl (Fmoc) peptide synthesis using reagents from Sigma-Aldrich and Iris and performed on acid-soluble Fmoc-β-Alanine etherified cellulose disks (area 0.12 cm^2, loading 1.0 µmol cm^{-2}). N-terminal Fmoc protection was removed by adding 2 µl and 4 µl 20% Piperidine in N-Methyl Pyrrolidone (NMP) for 5 and 10 min. Four couplings (10, 20, 30 and 40 min) using Oxyma/N,N′-Diisopropylcarbodiimide/Amino Acid in the relation (1.1/1.5/1.0) in at least 5-fold excess followed by two washing steps (100 µl and 300 µl NMP) and 4 µl capping solution (5% Acetic Anhydride in NMP) achieved peptide elongation by one amino acid. The subsequent peptide work-up was performed manually on all peptides in parallel after transfer of the cellulose disks into 96 deep-well blocks. Peptide side-chain deprotection was achieved with 150 µl deprotection solution (trifluoroacetic acid/triisopropylsilane/water/DCM: 80%, 3%, 5%, 12%) for 2 h. Disks were then solubilized overnight in 250 µl of cellulose solvation solution (trifluoroacetic acid/trifluoromethansulfonic acid/triisopropylsilane/water: 88.5%, 4%, 2.5%, 5%) under strong agitation. 750 µl Diethylether (-20° C) was added to the dissolved cellulose−peptide conjugates. The mixture was briefly agitated and kept at -20 °C for 1 h. Precipitated conjugates were pelleted by centrifugation at 2,000 rcf for 30 min at 4 °C. After removal of the supernatant the pellet was additionally washed twice with 750 µl fresh Diethylether (-20° C). After the final washing step, residual ether was evaporated and 250 µl of dimethyl sulfoxide (DMSO) was added to re-

solvate the cellulose-peptide conjugates. The cellulose-peptide conjugate stock solutions were stored at -20 °C. Prior printing 80 µl of the stocks were transferred to a 384-well plate, and mixed with 20 µl SSC buffer (150 NaCl; 15 µM $Na_3C_6H_5O_7$; pH 7.0). 50 nl of each peptide was contact printed on coated glass slides with a slide spotting robot (Intavis AG). After drying overnight, peptide microarrays were washed, equilibrated and blocked with 2 x 2 ml array buffer (0.01 M phosphate buffered saline (NaCl 138 mM; KCl 2.7 mM); pH 7.4, 0.05% bovine serum albumin). Arrays were incubated with 2 ml Aurora-A kinase at 4 °C for 1 h. After washing with 4 x 2 ml array buffer the arrays were incubated with 2 ml array buffer and horse radish peroxidase (HRP) coupled anti-His antibody (Thermo Fisher Scientific, MA1-21315-HRP, dilution 1:20,000). Aurora-A kinase binding was visualized after washing with 4 x 2 ml array buffer with 300 µl ECL Western Blotting Substrate (Thermo Fisher Scientific). Prepared microarrays were imaged using the GeneSys Pxi system (Syngene). The resulting images were analyzed using the Active Motif software. For all peptide array data sets >95% of the peptide SPOTs were within an <5% error margin when comparing intensities between peptide duplicates.

QUANTIFICATION AND STATISTICAL ANALYSIS

Bioinformatic analyses and statistics

Base calling was performed with Illumina's CASAVA software or FASTQ Generation software v1.0.0 and overall sequencing quality was tested using the FastQC script. For ChIP-sequencing, fastq files were mapped to the human genome (hg19) using Bowtie v1.1.1. (Langmead and Salzberg, 2012) with default parameters and normalized to the sample with the smallest number of mapped reads. Peaks were called using MACS v1.4.2 (Zhang et al., 2008) with a p-value cut-off of 1.0×10^{-6} (N-MYC, TFIIIC5), 1.0×10^{-11} (RAD21) or 1.0×10^{-12} (CTCF) and the input sample as control. Wiggle files were generated using MACS, bedGraph files were generated using the genomecov function from BEDTools and the Integrated Genome Browser (Nicol et al., 2009) was used to visualize density files. Heat maps illustrating DNA binding were calculated using DeepTools (Ramirez et al., 2016) with a resolution of 50 bp. Overlapping N-MYC/TFIIIC binding sites were determined using the intersectBed function from BEDTools (Quinlan, 2014) with a minimum overlap of 1 bp and corresponding p-values were calculated using a permutation test with 1.0×10^{6} iterations. Genes were assigned to be bound by N-MYC or TFIIIC, if a peak was called within a region of +/-1 kb around a transcriptional start site.

N-MYC binding sites were generated by intersecting N-MYC peaks in DMSO and CD532 using bedtools with a minimum overlap of 1 bp leading to 10,157 peaks. TFIIIC5 reads in +CD532 sample were counted in a region of +/-100 bp around the N-MYC peak summit and binding sites with less then 8 reads were defined as N-MYC-only sites. Only binding sites that were within +/-1 kb around a transcriptional start site of an RNAPII transcribed gene were considered. To determine the occupancy of N-MYC, TFIIIC5, CTCF and RAD21 the number of reads was counted in a region of +/-100 bp around the N-MYC peak summit.

Changes in N-MYC and TFIIIC occupancy upon CD532 treatment at N-MYC/TFIIIC peaks was calculated by counting tags in a region of 50 bp around the N-MYC peak, p-values were calculated using a two-tailed one-sample Wilcoxon signed-rank test. Occupancy at promoters of selected gene sets was measured by counting tags in a region of +/-0.5 kb

around the TSS and corresponding p-values were calculated by a two-tailed, paired Wilcoxon signed-rank test.

For *de novo* motif analyses of N-MYC and TFIIIC peaks the MEME and DREME algorithms implemented in the MEME Suite (Bailey et al., 2009) were used with an input region of +/- 50 bp around the peak summit. To compute occurrences of pre-defined motifs (E-box: CACGTG, CTCF: MA0139.1, AP2a: MA0003.2) the CENTRIMO tool was used: the frequency of a motif at a certain position was normalized to the number of input sequences and a rolling mean of 20 bp was applied for smoothing the curves.

RNAPII occupancy was calculated by counting reads in promoters (-30 bp to +300 bp relative to TSS), gene bodies (+300 bp to TES) and TES (TES to +1 kb), addition of one pseudocount/kb and normalization to region length. The traveling ratio is defined as occupancy in promoter divided by occupancy in gene body (Rahl et al., 2010). For the analyses only expressed/RNAPII-bound genes were used (2D Kernel density plots: >20 RNAPII counts/kb in promoters; bin plots: $\log_2$CPM >1.28). 2D Kernel density plots were generated with the smoothScatter function in R and default settings, bin plots were generated by calculating the mean of equal-sized bins. Metagene window plots were produced using ngs.plot (Shen et al., 2014) and all annotated genes from the UCSC RefSeq list.

For RNA-sequencing, reads were mapped to hg19 with TopHat2 (Kim et al., 2013) and Bowtie1 with default settings. Reads per gene were counted using the countOverlaps function from the R package *GenomicRanges*. Weakly expressed genes (mean count over all samples <1.5) were removed and differentially expressed genes were called using EdgeR. For Venn diagrams, genes were filtered based on $\log_2$FC threshold of |0.5| (siTFIIIC5 vs siCtr) or |1.0| (siRAD21 vs siCtr). Statistical significant overlap of regulated genes presented in Venn diagrams were calculated using a Monte-Carlo simulation with 100,000 iterations and 17,450 genes as population size. The p-values were calculated as (r+1)/(n+1) with r as the number of iterations producing a greater or equal overlap than the actual one and n as the total number of iterations (North et al., 2002). GSE analyses (Subramanian et

al., 2005) were performed with signal2noise metric, 1,000 permutations and the C2 gene set collection of MSigDB. To measure gene expression changes in N-MYC depleted neuroblastoma cells (GSE39218, samples with double infection) raw data were downloaded, RMA-normalized, probes to genes collapsed by mean and $\log_2$ fold changes were calculated. Association of gene expression of specific gene sets in human neuroblastoma was determined as described previously (von Eyss et al., 2015). Expression data at different stages were downloaded from GEO (GSE16476), RMA-normalized and the association score was calculated using a custom R script using the following formula: -log10 p-value x direction. Here, -1 means a negative and +1 a positive association. Box and whisker plots are characterized by a horizontal line reflecting the median, boxes spanning the first and third quartile and whiskers expanding to 1.5x interquartile range of the first and third quartile, respectively. Outliers are shown as individual dots, p-values comparing medians in box plots are calculated with one- or two-sample two-tailed Wilcoxon Signed-rank tests. For binned data the mean of each bin is plotted.

Statistical significance between experimental groups were determined by Student's t test or, when means of three or more groups were compared, by one-way ANOVA. Data analysis was performed with Prism5.0 Software (GraphPad). P values < 0.05 were considered statistically significant.

DATA AND SOFTWARE AVAILABILITY

ChIP- and RNA-sequencing datasets are available at the Gene Expression Omnibus under the accession number GEO: GSE78957. The authors do not declare a conflict of interest

Resource Table

REAGENT or RESOURCE	SOURCE	IDENTIFIER
Antibodies		
Actin beta (mouse)	Sigma-Aldrich	Clone: AC15 Cat# A5441
Aurora-A/AIK antibody (rabbit)	Cell Signaling	Cat# 3092
Aurora-A (rabbit)	Genetex	Clone: C3 Cat# GTX104620
Aurora-A (mouse)	Sigma-Aldrich	Clone: 35C1 Cat#A1231
Aurora-A (goat)	Santa Cruz	Clone: N-20 Cat# sc-14318
pT288 Aurora-A (rabbit)	Cell Signaling	Cat# 2914
ATM pS1981 (mouse)	Millipore	Clone: 10H11.E12 Cat# MAB3806
CDK2 (rabbit)	Santa Cruz	Clone: M-2 Cat# sc-163
CTCF (rabbit)	Abcam	Cat# ab70303
FLAG-tag (mouse)	Sigma-Aldrich	Clone: M2 Cat# F1804
HA-tag (rabbit)	Abcam	Cat# ab9110
N-MYC (mouse)	Santa-Cruz	Clone: B8.4.B Cat# sc-53993
N-MYC (mouse)	Calbiochem	Clone: NCM II 100 Cat# OP13
P400 (rabbit)	Abcam	Cat# ab5201
RAD21 (rabbit)	Bethyl	Cat# A300-080A
TFIIIC1 (mouse)	Santa Cruz	Clone: F-12 Cat# sc-398780
TFIIIC2 (mouse)	Abcam	Cat# ab89113
TFIIIC5 (rabbit)	Bethyl	Cat# A301-242A
TRRAP (rabbit)	Abcam	Cat# ab73546
TOP1 (rabbit)	Bethyl	Cat# A302-589A
TOP2A (rabbit)	Bethyl	Cat# A300-054A
TOP2B (rabbit)	Bethyl	Cat# A300-949A
Tubulin beta (mouse)	Millipore	Clone: TU-20 Cat# MAB1637
Vinculin (mouse)	Sigma-Aldrich	Clone: hVin-1 Cat# V9131
RPA32 (mouse)	Santa Cruz	Clone: MA34 Cat# sc-53496

RPA32 pS33 (rabbit)	Bethyl	Cat# A300-246A
RPA32 pS4/8 (rabbit)	Bethyl	Cat# A300-245A
CHK1 (rabbit)	Santa Cruz	Clone: FL-476 Cat# sc-7898
pS345 CHK1 (rabbit)	Cell Signaling	Clone: 133D3 Cat#2348
P53 (mouse)	Millipore	Clone: pAb1801 #Cat OP09
BRCA1 (rabbit)	Bethyl	Cat# A300-000A
RPA70 (mouse)	Millipore / Calbiochem	Clone: RPA34-20 Cat# NA19L
CDC73 (rabbit)	Bethyl	Cat# A300-170A
CTR9 (rabbit)	Bethyl	Cat# A301-395A
TRRAP (rabbit)	Bethyl	Cat# A310-373A
FITC anti-BrdU, Mouse IgG1, kappa	Biozol / BioLegend	Clone: 3D4 Cat# BLD-364104
RNA polymerase II (rabbit)	Santa Cruz	Clone: N-20 Cat# sc-899
RNA polymerase II CTD repeat YSPTSPS (phospho Ser2) (rabbit)	Abcam	Cat# ab5095
RNA polymerase II (hypo-phosphorylated) (mouse)	Santa Cruz	Clone: 8WG16 Cat# sc-56767
RNA polymerase II (phospho Ser5) (mouse)	BioLegend / previous Covance	Clone: CTD4H8 Cat# MMS-128P
Anti-rabbit HRP	Amersham	Cat# NA934
Anti-mouse HRP	Amersham	Cat# NA931
Rabbit TrueBlot	Rockland	Clone: eB182 Cat# 18-8816-33
Mouse TrueBlot	Rockland	Clone: eB182 Cat# 18-8816-33
IRDye® 800CW Donkey anti-Mouse IgG (H + L)	LI-COR Biosciences GmbH	Cat# 926-32212
IRDye® 800CW Donkey anti-Rabbit IgG (H + L)	LI-COR Biosciences GmbH	Cat# 926-32213
6x-His Tag Monoclonal Antibody (mouse)	Thermo Fisher Scientific	Clone: HIS.H8 Cat# MA1-21315
Chemicals, Peptides, and Recombinant Proteins		
MK-5108	Selleckchem	Cat# S2770
MLN8237	Selleckchem	Cat#S1133
CD532	R. Bayliss	N/A

CD532	Calbiochem / Merck	Cat# 532605
Thymidine	Sigma-Aldrich	Cat# T9250
3x FLAG-peptide	Sigma-Aldrich	Cat# F4799
Aurora-A protein	Burgess and Bayliss, 2015	N/A
Hoechst 33342	Sigma-Aldrich	Cat# B2261
4-Hydroxytamoxifen	Sigma-Aldrich	Cat# H7904-5MG
Puromycin	InvivoGen	Cat# ant-pr-1
MG-132	Calbiochem	Cat# 474790-20MG
Polybrene	Sigma-Aldrich	Cat# 107689-100G
Dynabeads® Protein A	Life Technologies GmbH	Cat# 10002D
Dynabeads® Protein G	Life Technologies GmbH	Cat# 10004D
Pierce® Anti-HA Agarose	Pierce	Cat# 26181
Pierce® HA Peptide	Pierce	Cat# 26184
Formaldehyde (37%)	Roth	Cat# 4979.1
Crystal Violet	Sigma-Aldrich	Cat# C0775-25G
Critical Commercial Assays		
Duolink® In Situ PLA® Probe Anti-Rabbit PLUS, Affinity purified Donkey anti-Rabbit IgG (H+L)	Sigma-Aldrich	DUO92002
Duolink® In Situ PLA® Probe Anti-Mouse MINUS, Affinity purified Donkey anti-Mouse IgG (H+L)	Sigma-Aldrich	DUO92004
Duolink® In Situ Detection Reagents Red	Sigma-Aldrich	DUO92008
Duolink® In Situ Wash Buffers, Fluorescence	Sigma-Aldrich	DUO82049
Rneasy Mini Kit	Qiagen	74106
Rnase-free Dnase kit	Qiagen	79254
MiniElute PCR Purification Kit	Qiagen	28006
QIAquick PCR Purification Kit	Qiagen	28106
QIAquick Gel Extraction Kit	Qiagen	28704
Experion RNA StdSense kit	Bio-Rad	700-7103
Experion DNA 1K Kit	Bio-Rad	700-7307
NEBNext® Ultra™ RNA Library Prep Kit for Illumina	NEB	E7530 L
NEBNext Poly(A) mRNA Magnetic Isolation Module	NEB	E7490 L
NEBNext® ChIP-Seq Library Prep Master Mix Set for Illumina®	NEB	E6240 L
NEBNext® Multiplex Oligos for Illumina® (Dual Index Primers Set 1)	NEB	E7600 S
NextSeq® 500/550 High Output Kit v2 (75 cycles)	Illumina	FC-404-2005

Quant-iT™ Pico Green®	Thermo Fisher Scientific Inc.	Cat# P7589
ABsolute QPCR SYBR Green Mix (no ROX)	Thermo Fisher Scientific	Cat# AB-1158/B
PowerUp™ SYBR® Green Master Mix	Thermo Fisher Scientific	Cat# A25778
Deposited Data		
Raw and analyzed data	This paper	GEO: GSE78957
Raw data N-MYC depleted neuroblastoma cells	Valentijn LJ et al., 2012	GEO: GSE39218
Expression data at different stages of neuroblastoma	R. Versteeg	GEO: GSE16476
Experimental Models: Cell Lines		
Human neuroblastoma: IMR-5	A. Eggert	N/A
Human neuroblastoma: IMR-32	M. Schwab	N/A
Human neuroblastoma: SH-EP	M. Schwab	N/A
Human neuroblastoma: SH-EP NMYCER	M. Eilers	N/A
Pseudoviral Particle Producer cell line: HEK293TN	ATCC	Cat# CRL-11268
Retroviral Packaging cell line: PlatE	B. v. Eyss	N/A
Recombinant DNA		
pInducer-11	Addgene	Cat# 44363 Meerbrey et al., 2011
psPAX.2	Addgene	Cat# 12260 D. Trono
pMD2.G	Addgene	Cat# 12259 D. Trono
pETM6T1	R. Bayliss	N/A
lentiCRISPR v2	Addgene	Cat# 52961 Sanjana et al., 2014
Sequence-Based Reagents		
ON-TARGETplus SMARTpools GTF3C5	GE Healthcare	L-020031-00-0005
ON-TARGETplus SMARTpools RAD21	GE Healthcare	L-006832-00-0005
ON-TARGETplus non-targeting control pool	GE Healthcare	D-001810-10-20
shRNA targeting TFIIIC5: AAGCGCAGCACCTACAACTACA	(Fellmann et al., 2013)	shRNA ID: GTF3C5.1361
shRNA targeting TFIIIC2: TCCGTAGAGATGTCATTACCTA	Fellmann et al., 2013	shRNA ID: GTF3C2.435

shRNA targeting N-MYC: GAGGAGCATGTTTTGTATACAA	Fellmann et al., 2013	shRNA ID: MYCN.2214
Primers for ChIP, see Supplemental Experimental Procedures	This paper	N/A
gRNA for CRISPR, see Supplemental Experimental Procedures	Hart et al., 2015	N/A
Software and Algorithms		
Bowtie v1.1.1	Langmead and Salzberg, 2012	
MACS v1.4.2	Zhang et al., 2008	
Integrated Genome Browser	Nicol et al., 2009	
SeqMINER	Ye et al., 2014	
BEDTools	Quinlan, 2014	
MEME Suite	Bailey et al., 2009	
TopHat2	Kim et al., 2003	
GSEA	Subramanian et al., 2005	
DeepTools	Ramirez et al., 2016	
Ngs.plot	Shen et al., 2014	
Prism5.0 Software	GraphPad	

References

BAILEY, T. L., BODEN, M., BUSKE, F. A., FRITH, M., GRANT, C. E., CLEMENTI, L., REN, J., LI, W. W. & NOBLE, W. S. 2009. MEME SUITE: tools for motif discovery and searching. *Nucleic Acids Res,* 37**,** W202-8.

BAYLISS, R., SARDON, T., VERNOS, I. & CONTI, E. 2003. Structural basis of Aurora-A activation by TPX2 at the mitotic spindle. *Mol Cell,* 12**,** 851-62.

BURGESS, S. G. & BAYLISS, R. 2015. The structure of C290A:C393A Aurora A provides structural insights into kinase regulation. *Acta Crystallogr F Struct Biol Commun,* 71**,** 315-9.

CHEN, X., XU, H., YUAN, P., FANG, F., HUSS, M., VEGA, V. B., WONG, E., ORLOV, Y. L., ZHANG, W., JIANG, J., LOH, Y. H., YEO, H. C., YEO, Z. X., NARANG, V., GOVINDARAJAN, K. R., LEONG, B., SHAHAB, A., RUAN, Y., BOURQUE, G., SUNG, W. K., CLARKE, N. D., WEI, C. L. & NG, H. H. 2008. Integration of external signaling pathways with the core transcriptional network in embryonic stem cells. *Cell,* 133**,** 1106-17.

COX, J. & MANN, M. 2008. MaxQuant enables high peptide identification rates, individualized p.p.b.-range mass accuracies and proteome-wide protein quantification. *Nat Biotechnol,* 26**,** 1367-72.

FELLMANN, C., HOFFMANN, T., SRIDHAR, V., HOPFGARTNER, B., MUHAR, M., ROTH, M., LAI, D. Y., BARBOSA, I. A., KWON, J. S., GUAN, Y., SINHA, N. & ZUBER, J. 2013. An optimized microRNA backbone for effective single-copy RNAi. *Cell Rep,* 5**,** 1704-13.

HART, T., CHANDRASHEKHAR, M., AREGGER, M., STEINHART, Z., BROWN, K. R., MACLEOD, G., MIS, M., ZIMMERMANN, M., FRADET-TURCOTTE, A., SUN, S., MERO, P., DIRKS, P., SIDHU, S., ROTH, F. P., RISSLAND, O. S., DUROCHER, D., ANGERS, S. & MOFFAT, J. 2015. High-Resolution CRISPR Screens Reveal Fitness Genes and Genotype-Specific Cancer Liabilities. *Cell,* 163**,** 1515-26.

JAENICKE, L. A., VON EYSS, B., CARSTENSEN, A., WOLF, E., XU, W., GREIFENBERG, A. K., GEYER, M., EILERS, M. & POPOV, N. 2016. Ubiquitin-Dependent Turnover of MYC Antagonizes MYC/PAF1C Complex Accumulation to Drive Transcriptional Elongation. *Mol Cell,* 61**,** 54-67.

KIM, D., PERTEA, G., TRAPNELL, C., PIMENTEL, H., KELLEY, R. & SALZBERG, S. L. 2013. TopHat2: accurate alignment of transcriptomes in the presence of insertions, deletions and gene fusions. *Genome Biol,* 14**,** R36.

LANGMEAD, B. & SALZBERG, S. L. 2012. Fast gapped-read alignment with Bowtie 2. *Nat Methods,* 9**,** 357-9.

NICOL, J. W., HELT, G. A., BLANCHARD, S. G., JR., RAJA, A. & LORAINE, A. E. 2009. The Integrated Genome Browser: free software for distribution and exploration of genome-scale datasets. *Bioinformatics,* 25**,** 2730-1.

NORTH, B. V., CURTIS, D. & SHAM, P. C. 2002. A note on the calculation of empirical P values from Monte Carlo procedures. *Am J Hum Genet,* 71**,** 439-41.

QUINLAN, A. R. 2014. BEDTools: The Swiss-Army Tool for Genome Feature Analysis. *Curr Protoc Bioinformatics,* 47**,** 11 12 1-11 12 34.

RAHL, P. B., LIN, C. Y., SEILA, A. C., FLYNN, R. A., MCCUINE, S., BURGE, C. B., SHARP, P. A. & YOUNG, R. A. 2010. c-Myc regulates transcriptional pause release. *Cell,* 141**,** 432-45.

RAMIREZ, F., RYAN, D. P., GRUNING, B., BHARDWAJ, V., KILPERT, F., RICHTER, A. S., HEYNE, S., DUNDAR, F. & MANKE, T. 2016. deepTools2: a next generation web server for deep-sequencing data analysis. *Nucleic Acids Res,* 44**,** W160-5.

SCHULEIN-VOLK, C., WOLF, E., ZHU, J., XU, W., TARANETS, L., HELLMANN, A., JANICKE, L. A., DIEFENBACHER, M. E., BEHRENS, A., EILERS, M. & POPOV, N. 2014. Dual regulation of fbw7 function and oncogenic transformation by usp28. *Cell Rep,* 9**,** 1099-109.

SHEN, L., SHAO, N., LIU, X. & NESTLER, E. 2014. ngs.plot: Quick mining and visualization of next-generation sequencing data by integrating genomic databases. *BMC Genomics,* 15**,** 284.

SUBRAMANIAN, A., TAMAYO, P., MOOTHA, V. K., MUKHERJEE, S., EBERT, B. L., GILLETTE, M. A., PAULOVICH, A., POMEROY, S. L., GOLUB, T. R., LANDER, E. S. & MESIROV, J. P. 2005. Gene set enrichment analysis: a knowledge-based approach for interpreting genome-wide expression profiles. *Proc Natl Acad Sci U S A,* 102**,** 15545-50.

VON EYSS, B., JAENICKE, L. A., KORTLEVER, R. M., ROYLA, N., WIESE, K. E., LETSCHERT, S., MCDUFFUS, L. A., SAUER, M., ROSENWALD, A., EVAN, G. I., KEMPA, S. & EILERS, M. 2015. A MYC-Driven Change in Mitochondrial Dynamics Limits YAP/TAZ Function in Mammary Epithelial Cells and Breast Cancer. *Cancer Cell,* 28**,** 743-57.

WALZ, S., LORENZIN, F., MORTON, J., WIESE, K. E., VON EYSS, B., HEROLD, S., RYCAK, L., DUMAY-ODELOT, H., KARIM, S., BARTKUHN, M., ROELS, F., WUSTEFELD, T., FISCHER, M., TEICHMANN, M., ZENDER, L., WEI, C. L., SANSOM, O., WOLF, E. & EILERS, M. 2014. Activation and repression by oncogenic MYC shape tumour-specific gene expression profiles. *Nature,* 511**,** 483-7.

YE, T., RAVENS, S., KREBS, A. R. & TORA, L. 2014. Interpreting and visualizing ChIP-seq data with the seqMINER software. *Methods Mol Biol,* 1150**,** 141-52.

ZHANG, Y., LIU, T., MEYER, C. A., EECKHOUTE, J., JOHNSON, D. S., BERNSTEIN, B. E., NUSBAUM, C., MYERS, R. M., BROWN, M., LI, W. & LIU, X. S. 2008. Model-based analysis of ChIP-Seq (MACS). *Genome Biol,* 9**,** R137.

Figure S1 Büchel et al.

A

Gene name	log$_2$ Ratio wt vs. Ctr	log$_2$ Ratio mut vs. Ctr	Reference
MYCN	10.88	10.31	NA
EP400	8.99	8.47	Fuchs, M. et al., Cell (2001).
TRRAP	7.75	8.43	McMahon, S.B. et al., Cell (1998).
MAX	7.61	5.65	Blackwood, E.M. & Eisenman, R.N., Science (1991).
DMAP1	5.08	5.68	Cai, Y. et al., JBiolChem (2005).
BPTF	4.90	3.91	Richart, L. et al., Nat Commun (2016).
CDC73	4.14	4.29	Jaenicke, L.A. et al., Mol Cell (2016).
VPS72	3.70	3.81	Cai, Y. et al., JBiolChem (2005).
MYCBP2	3.33		Guo, Q. et al., PNAS (1998).
HCFC1	3.56	3.03	Thomas, L.R. et al., Oncogene (2016).
YEATS4	3.33	2.84	Piccinni, E. et al., Acta Biochim Pol (2011).
EPC1	3.08	2.37	Doyon, Y et al., Molecular and cellular biology (2004).
PAF1	2.77	2.66	Jaenicke, L.A. et al., Mol Cell (2016).
PLK1	2.34	2.96	Popov, N. et al., Nature cell biology (2010).
CCNT1	2.48		Eberhardy, S.R. & Farnham, P.J., JBiolChem (2002).
KAT5	2.41	2.40	Frank, S.R. et al., EMBO Rep (2003).
AURKA	2.25		Otto, T. et al., Cancer Cell (2009).
RUVBL2	1.46	1.50	Wood, M.A. et al., Mol Cell (2000).
RUVBL1	1.30	1.53	Wood, M.A. et al., Mol Cell (2000).

B

C
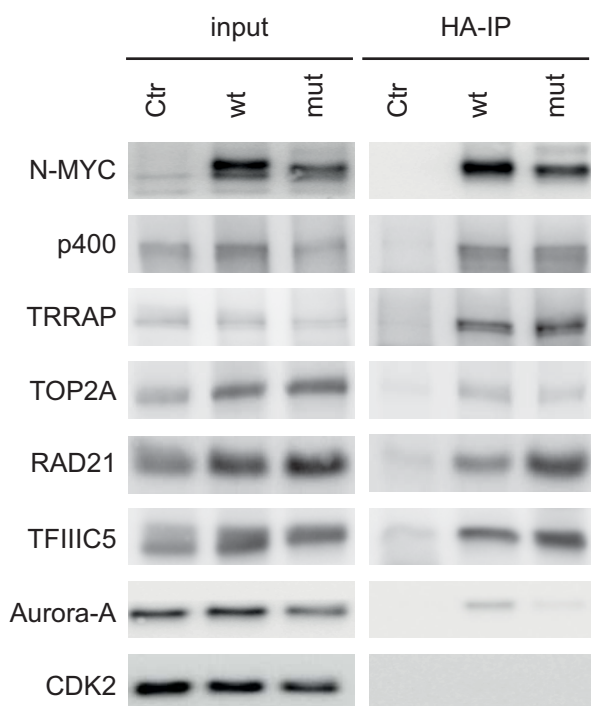
	Unique peptide counts	
Gene name	N-MYC IP	Ctr
MYCN	83	0
TRRAP	54	0
GTFIIIC1	39	0
HCFC1	15	0
GTFIIIC3	13	0
GTFIIIC4	8	0
GTFIIIC5	8	0
GTFIIIC2	7	2
TOP2A	4	0

D

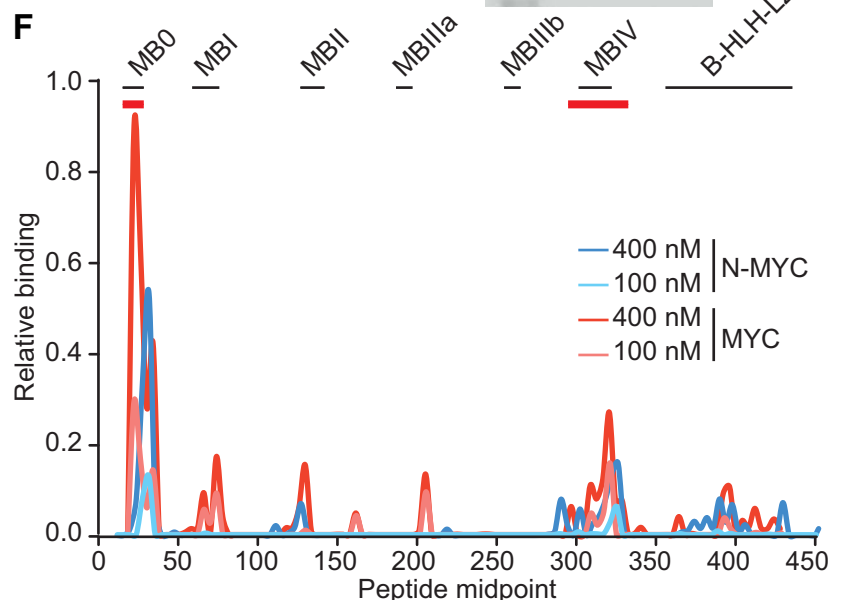|	Unique peptide counts	
Gene name	MYC IP	Ctr
MYC	30	1
TRRAP	109	2
GTFIIIC1	16	5
GTFIIIC3	10	2
GTFIIIC5	8	2
GTFIIIC2	5	3
TOP2A	23	10

E
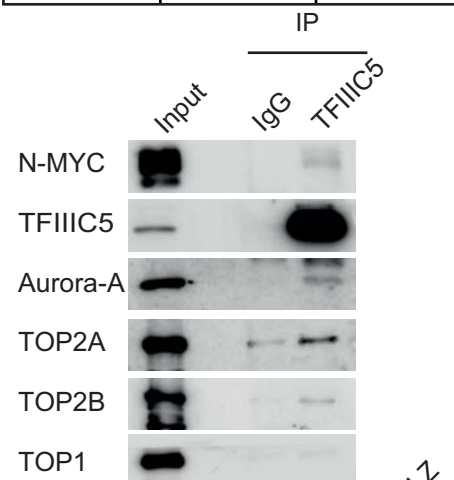
F

Figure S1: Related to Figure 1.

A. Table of previously identified protein-protein interactions of MYC and N-MYC proteins that were confirmed by our analysis. The table shows normalized $\log_2$ ratios of peptides purified from SH-EP cells expressing HA-tagged N-MYC$_{wt}$ (wt) or N-MYC$_{mut}$ (mut) relative to empty control vector (Ctr).

B. Immunoblots of α-HA immunoprecipitates from SH-EP cells expressing HA-tagged N-MYC$_{wt}$ or N-MYC$_{mut}$ or an empty control vector (Ctr). The input corresponds to 1% of the amount used for precipitation.

C. Table of mass spectrometry results of N-MYC immunoprecipitates from *MYCN*-amplified Kelly cells. Shown are peptide numbers of the indicated proteins.

D. Table of mass spectrometry results of MYC immunoprecipitates from U2OS cells expressing HA-tagged MYC. Shown are peptide numbers of the indicated proteins.

E. Immunoblots of α-TF3C5 immunoprecipitates from IMR-5 cells. The input corresponds to 1% of the amount used for precipitation. Non-specific IgG was used for control immunoprecipitation.

F. Peptide arrays showing binding of Aurora-A to peptide microarrays of N-MYC and MYC. 23mer peptides were spotted, each shifted by 5 amino acids. X-axis shows the position of peptide midpoints and the y-axis shows relative binding. Positions of conserved domains ("MYCboxes") are indicated at the top of the graph. Data are shown for two concentrations of Aurora-A.

A

B

C
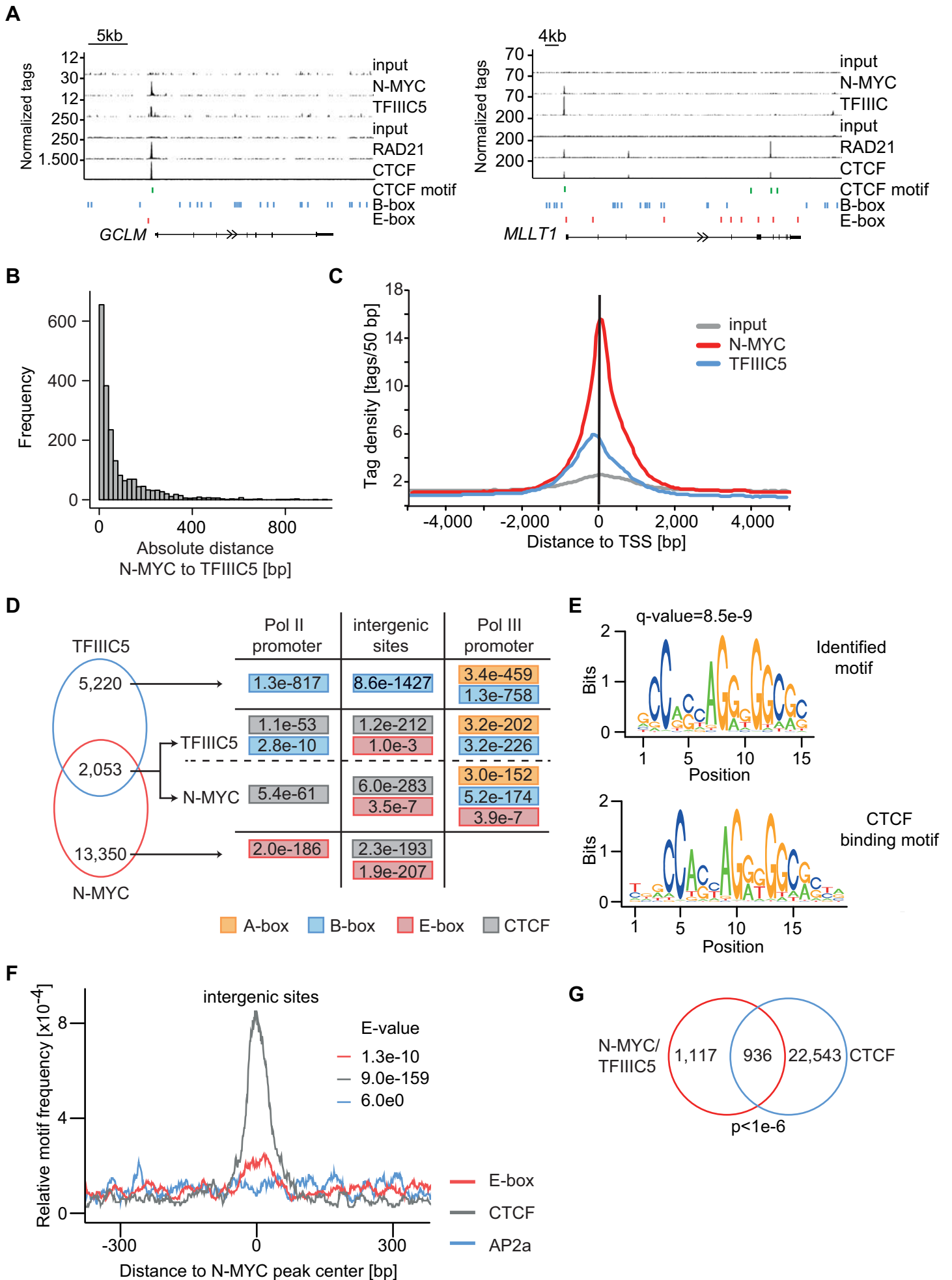

D

	Pol II promoter	intergenic sites	Pol III promoter
TFIIIC5 5,220	1.3e-817	8.6e-1427	3.4e-459
			1.3e-758
TFIIIC5	1.1e-53	1.2e-212	3.2e-202
2,053	2.8e-10	1.0e-3	3.2e-226
N-MYC	5.4e-61	6.0e-283	3.0e-152
		3.5e-7	5.2e-174
			3.9e-7
N-MYC 13,350	2.0e-186	2.3e-193	
		1.9e-207	

A-box | B-box | E-box | CTCF

E

q-value=8.5e-9

Identified motif

CTCF binding motif

F

G

Figure S2: Related to Figure 2.

A. Genome browser tracks at the *GCLM* and *MLLT1* loci illustrating DNA-binding of the indicated proteins. ChIP sequencing was performed on *MYCN*-amplified IMR-5 cells. The positions of B- and E-boxes and of CTCF motifs are indicated by vertical lines. Upper input is for ChIP sequencing of N-MYC and TFIIIC5, lower input for ChIP sequencing of RAD21 and CTCF.

B. Histogram demonstrating absolute distance between N-MYC and TFIIIC5 peak summits of N-MYC/TFIIIC5 joint peaks (n=2,053). The histogram is plotted at a resolution of 20 bp.

C. Tag density distribution of N-MYC and TFIIIC5 at overlapping sites around the transcription start site (TSS) of genes transcribed by Pol II.

D. *De novo* motif search in N-MYC- and/or TFIIIC5-bound regions. E-values were calculated using a binominal test and normalized to the number motifs in the database and are shown only if the respective motif was enriched in the bound sequences.

E. Sequence and q-value of the *de novo* identified motif in overlapping N-MYC/TFIIIC sites and comparison to a published CTCF motif (JASPAR MA0139.1).

F. Central enrichment of E-box, CTCF and AP2a (as negative control) motifs in the N-MYC peak of N-MYC/TFIIIC5 joint sites in intergenic sites. The E-value is calculated by a binominal test and adjustment for the number of motifs tested.
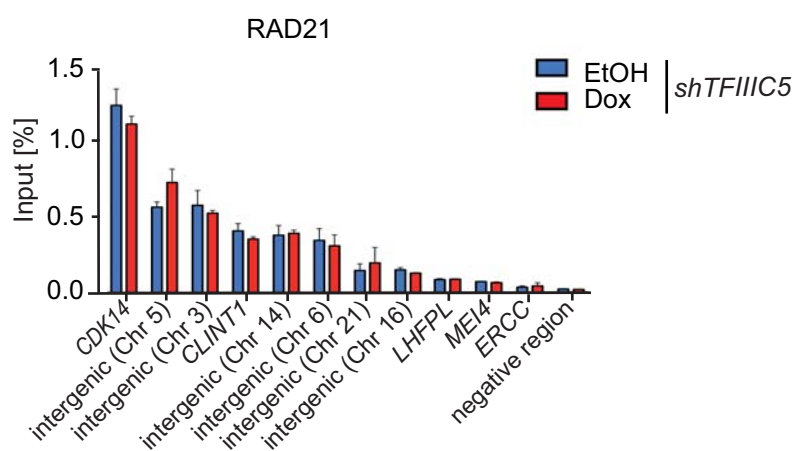
G. Venn diagram documenting genome-wide overlap of N-MYC/TFIIIC5 joint binding sites with CTCF. The p-value was calculated using a permutation test with 100,000 iterations.
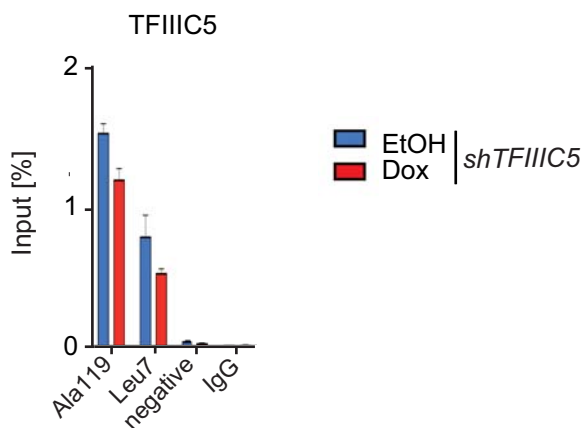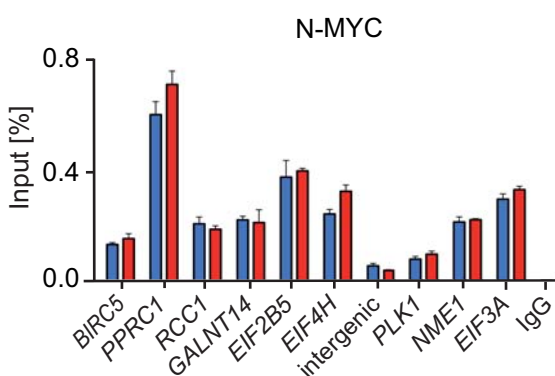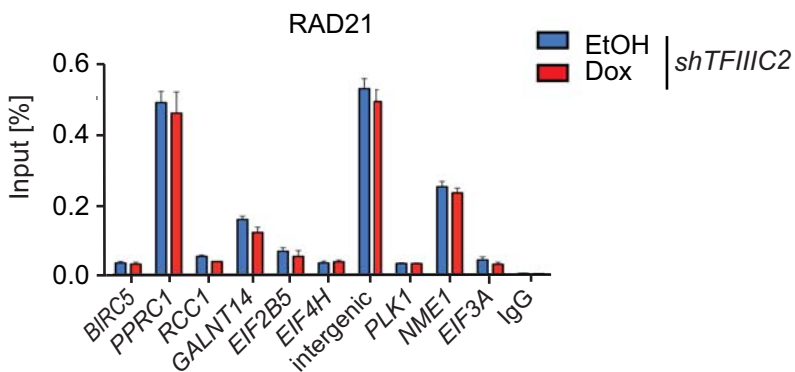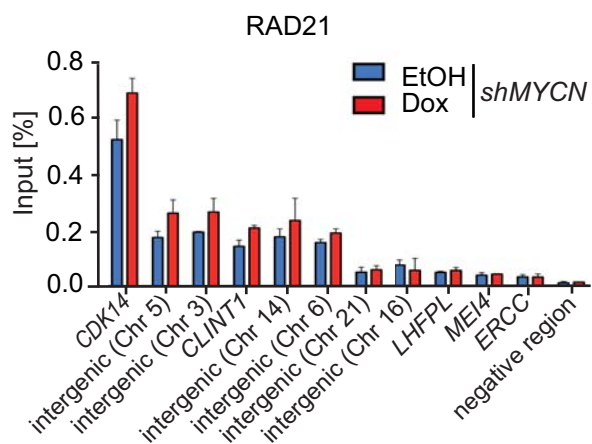
Figure S3 Büchel et al.
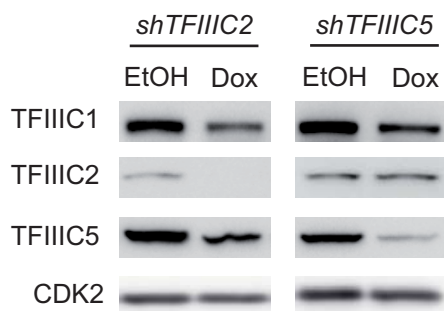
Figure S3: Related to Figure 3.

A. Immunoblot showing levels of the indicated proteins in response to depletion of TFIIIC2 or TFIIIC5. IMR-5 cells expressing an inducible shRNA directed against TFIIIC2 or TFIIIC5 were treated with doxycycline (Dox) for 48 hr or with ethanol (EtOH) as control.

B. ChIP experiment documenting binding of RAD21 to the indicated loci upon depletion of TFIIIC5. Error bars show SD of technical triplicates. These binding sites contain no detectable TFIIIC5 or N-MYC peak.

C. ChIP experiment showing binding of TFIIIC5 to tRNA genes upon depletion of TFIIIC5. Error bars show SD of technical triplicates from one experiment (n = 2).

D. ChIP experiment documenting binding of N-MYC and RAD21 to the indicated loci upon depletion of TFIIIC2. Error bars show SD of technical triplicates from one representative experiment (n = 3).

E. ChIP experiment documenting binding of RAD21 to the indicated loci upon depletion of N-MYC. Error bars show SD of technical triplicates. These binding sites contain no detectable TFIIIC5 or N-MYC peak

A

shTFIIIC5

IMR-5	SH-EP

EtOH

DOX

B

tRNA-Tyr

tRNA-Leu

EtOH
Dox

C

EV	gRNA #1	gRNA #2	gRNA #3

gRNA #5   gRNA #6   gRNA #7   gRNA #8

D

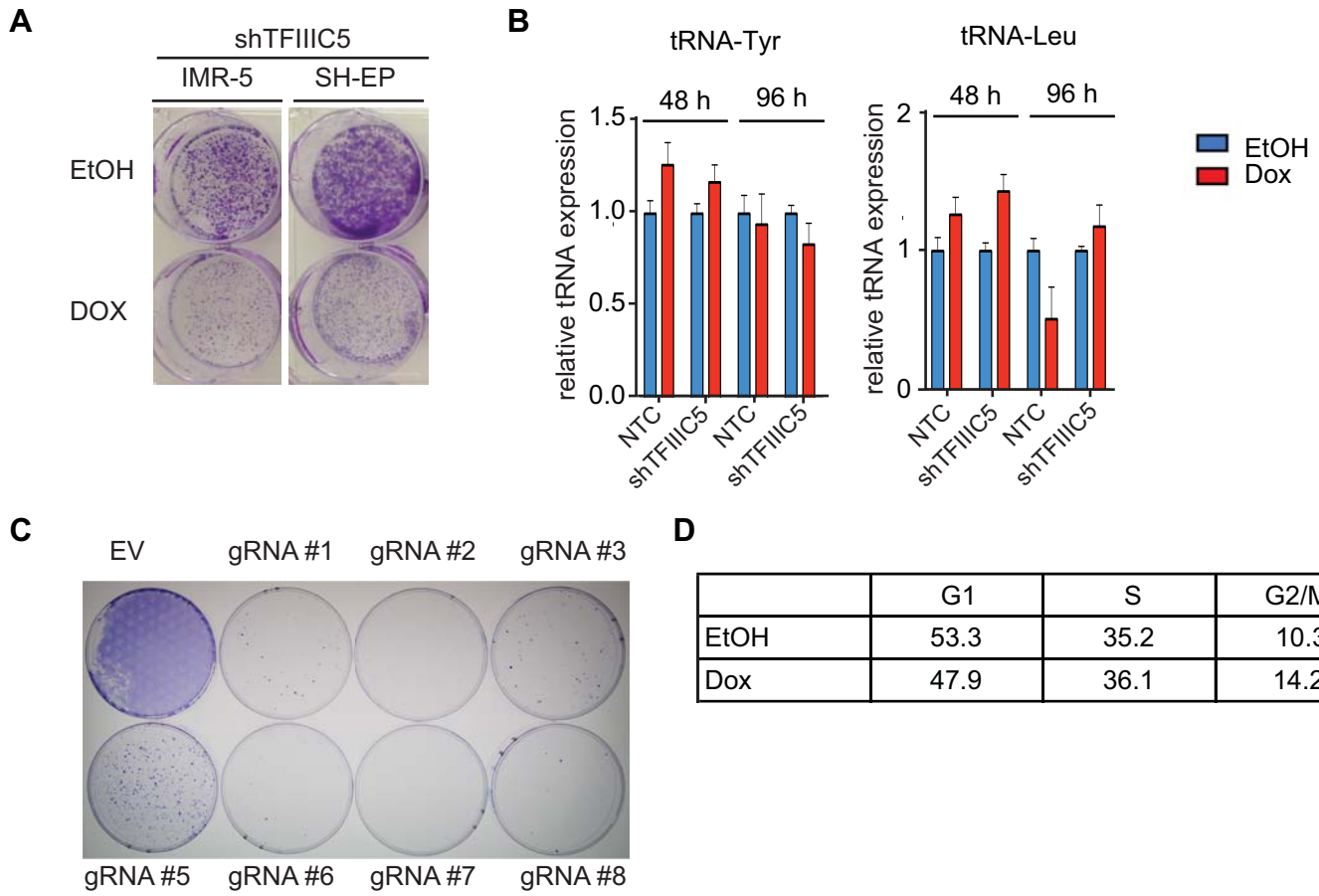|	G1	S	G2/M
EtOH	53.3	35.2	10.3
Dox	47.9	36.1	14.2

Figure S4: Related to Figure 4.

A. Clonogenic assay of IMR-5 and SH-EP neuroblastoma cells after shRNA-mediated knockdown of TFIIIC5. Colonies were stained with crystal violet.

B. Expression of indicated tRNAs in IMR-5 cells after shRNA-mediated depletion of TFIIIC5 or a non targeting control (NTC). Doxycycline or ethanol was added for 48 hr or 96 hr as indicated. Error bars show SD of technical triplicates.

C. Clonogenic assay of IMR-5 cells after sgRNA-mediated knockout of TFIIIC5. Colonies were stained with crystal violet. Multiple independent gRNA sequences were used.

D. Cell cycle distribution of IMR-5 cells after shRNA-mediated depletion of TFIIIC5. Data are taken from a propidium-iodide stained FACS experiment of cells before and 48 hr after addition of doxycycline.
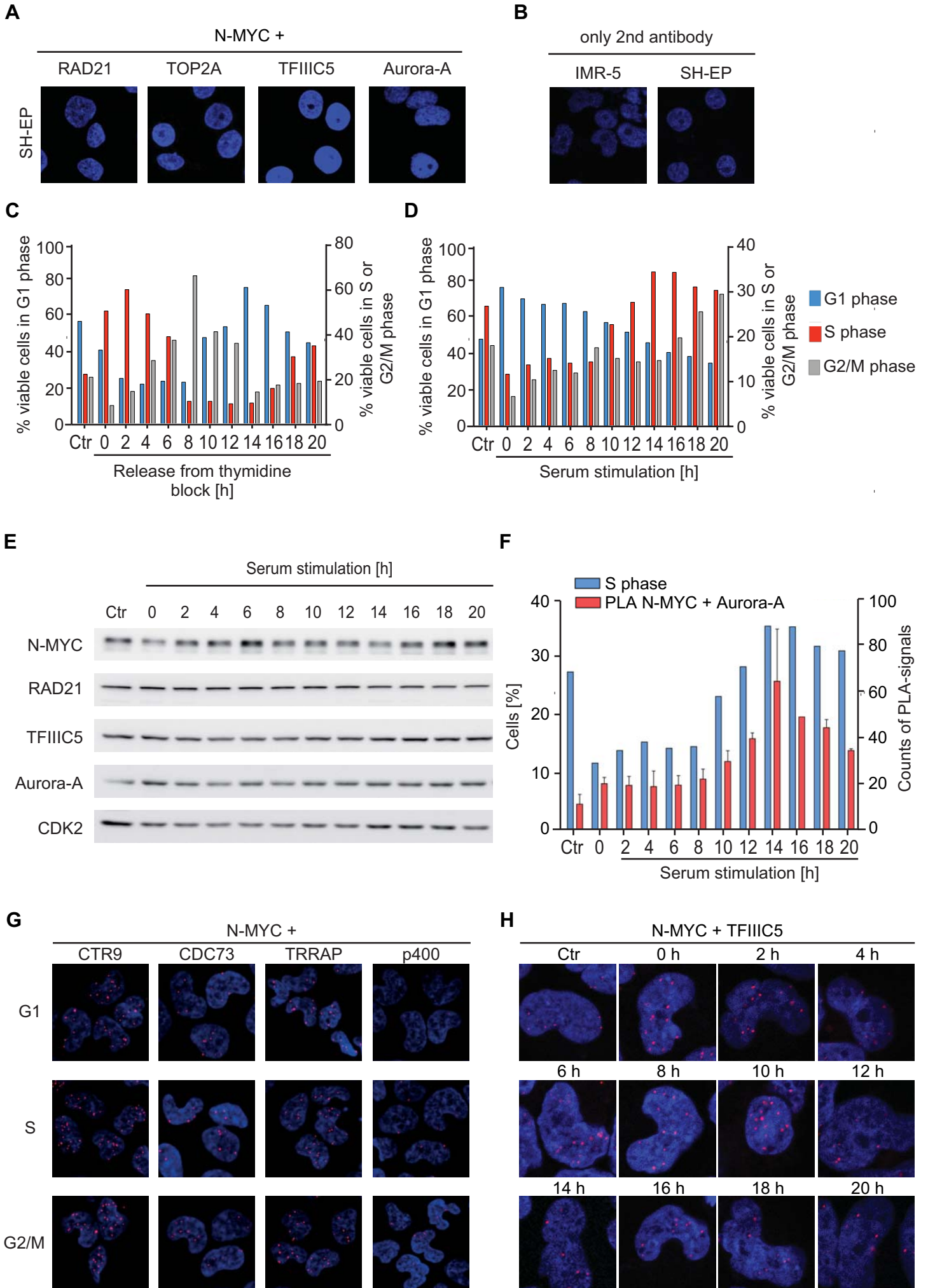
Figure S5 Büchel et al.

Figure S5: Related to Figure 5.

A. Negative controls for PLAs from SH-EP cells. The indicated antibodies were added to SH-EP cells that do not express N-MYC. Nuclei are stained using Hoechst.

B. Negative controls for PLAs from IMR-5 and SH-EP cells. The panels show PLA assays in which cells were incubated with secondary antibody only. Nuclei are stained using Hoechst.

C. Cell cycle distribution as determined by PI-FACS after release of IMR-5 cells from a double-thymidine block for the indicated times (n = 5). Left axis refers to viable cells in G1 phase shown in blue. Right axis refers to viable cells in S phase shown in red as well as G2/M phase shown in grey.

D. Cell cycle distribution as determined by PI-FACS after re-stimulation of serum-starved IMR-5 cells with 10% FCS (n = 5). Coloring is as in panel C.

E. Immunoblots documenting the levels of the indicated proteins re-stimulation of serum-starved IMR-5 cells with 10% FCS (n = 4).

F. Quantification of the PLA assay between N-MYC and Aurora-A after re-stimulation of serum-starved cells. The percentage of cells in S phase from one representative experiment is indicated in parallel. Error bars show SD of technical triplicates (n = 3).

G. The panels show representative pictures from PLAs documenting complex formation between N-MYC and the indicated proteins (n = 2). Nuclei are stained using Hoechst. Red dots show PLA signals resulting from interactions of N-MYC and the indicated proteins.

H. PLA assays documenting complex formation between N-MYC and TFIIIC5 after release from a double-thymidine block (n = 3). Nuclei are stained using Hoechst. Red dots show PLA signal for interaction of N-MYC and TFIIIC5.
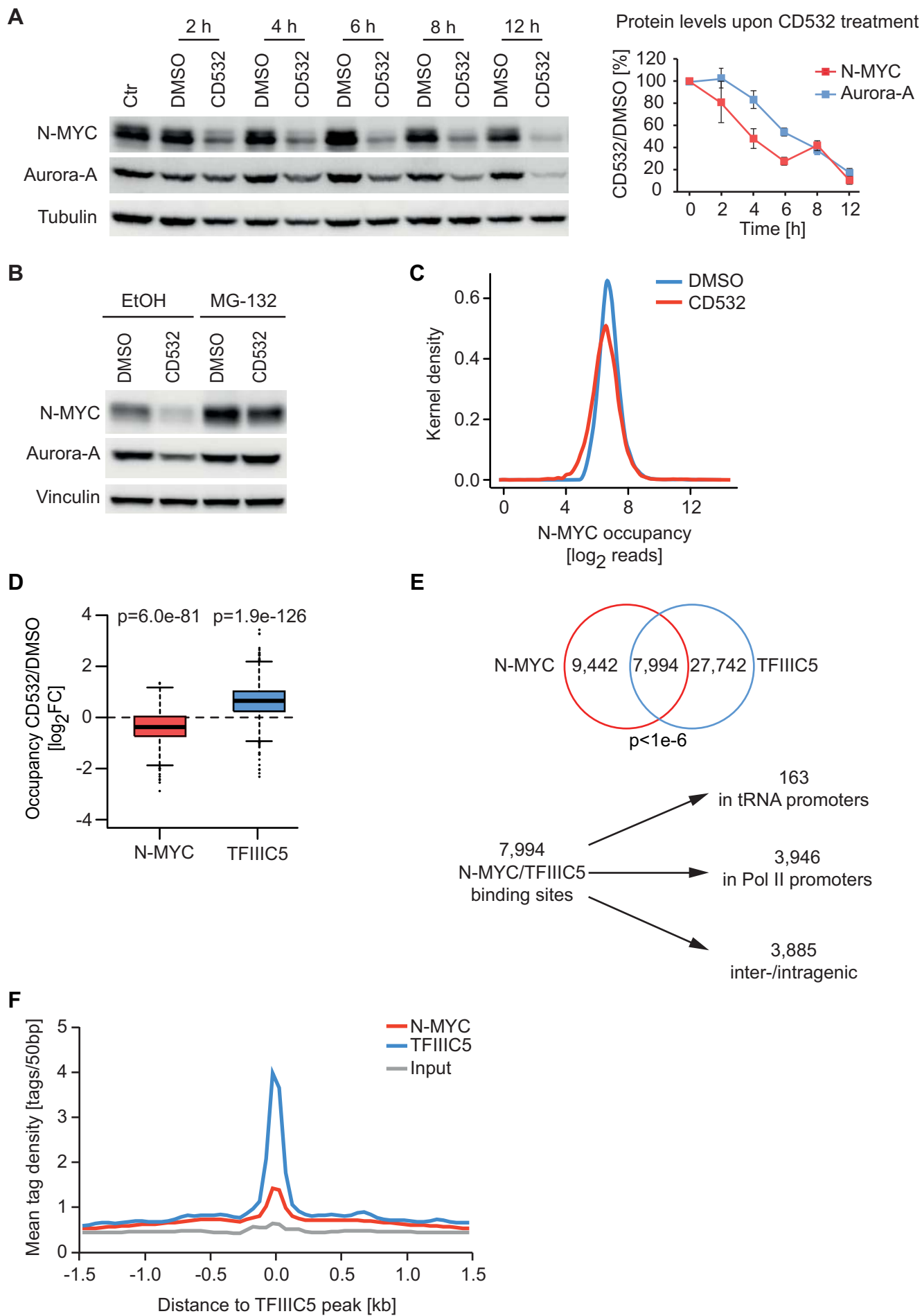
Figure S6 Büchel et al.

Figure S6: Related to Figure 6.

A. Immunoblots (left) and quantification (right) documenting decrease in overall N-MYC and Aurora-A levels after exposure of IMR-5 cells to CD532 (1 μM) for the indicated times. Error bars show SD (n = 3).

B. Immunoblot documenting levels of Aurora-A and N-MYC after 4 hr exposure to 1 μM of CD532 in the presence of the proteasome inhibitor MG-132 or ethanol (EtOH) as control (n = 2).

C. Change in N-MYC occupancy upon CD532 treatment of all N-MYC peaks (n=15,403). Reads were counted in a window of 250 bp around the peak summit, $\log_2$-transformed and the probability density estimation was calculated using a Gaussian kernel function with a bandwidth of 0.1.

D. Box plots documenting changes in N-MYC and TFIIIC5 occupancy at overlapping binding sites in Pol II promoters after exposure of non-synchronized IMR-5 cells to CD532 (4 hr; 1 μM).

E. Venn diagram documenting genome-wide overlap of N-MYC and TFIIIC5 in IMR-5 neuroblastoma cells after exposure to CD532. The p-value was calculated using a permutation test with 100,000 iterations (top). Diagram showing distribution of joint N-MYC/TFIIIC5 binding sites (bottom).

F. Mean tag density around 28,671 TFIIIC5 binding sites without an overlapping N-MYC peak. Tags were counted in a window of +/-1.5 kb around the TFIIIC5 peak summit at a resolution of 50 bp.
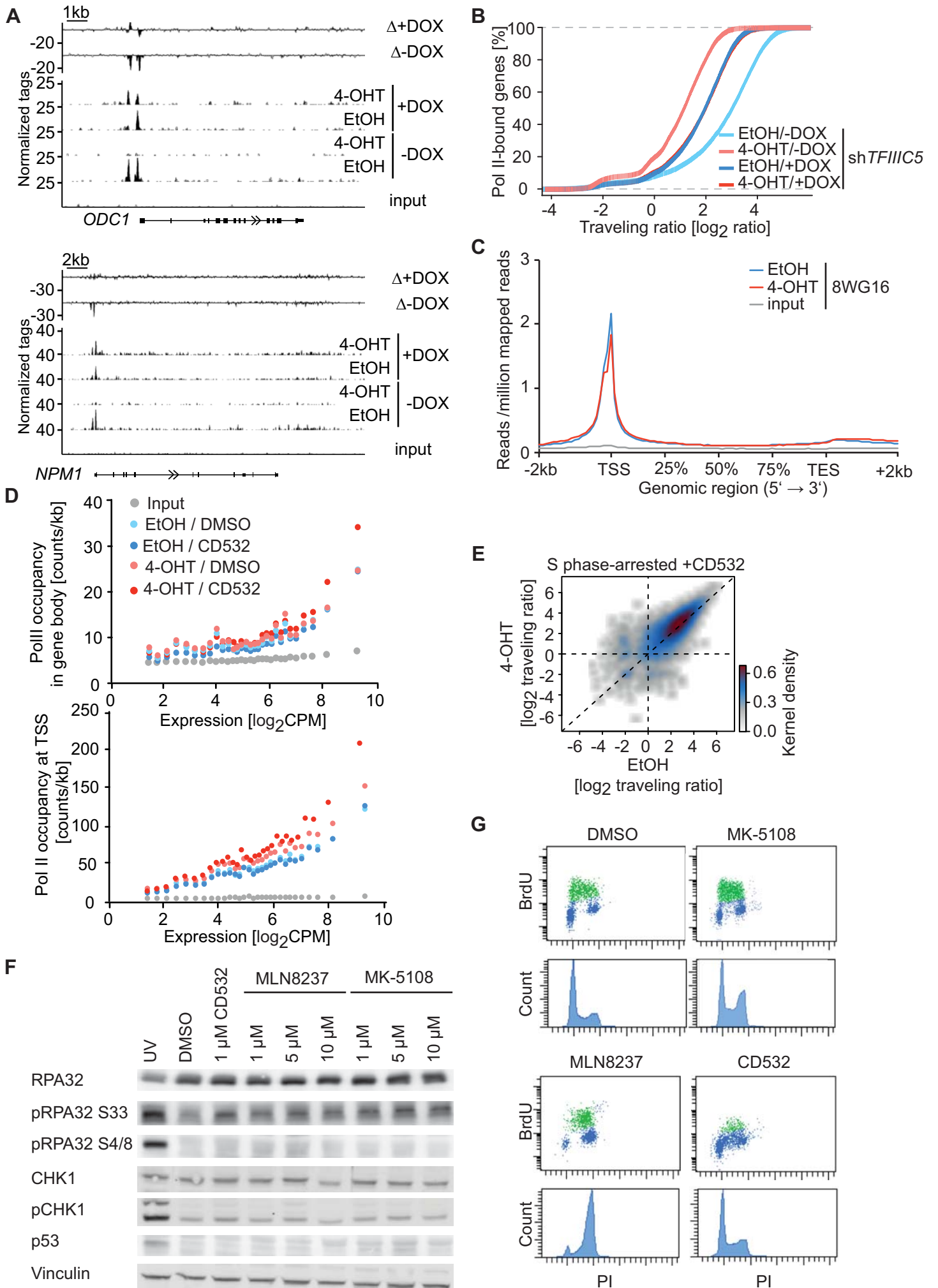
Figure S7: Related to Figure 7.

A. Browser plots showing Pol II occupancy at the indicated loci in SHEP-N-MYCER cells expressing a doxycycline-inducible shRNA targeting TFIIIC5. Doxycycline (1 µg ml^{-1}) was added for 30 hr where indicated, EtOH was used as control. The top two traces show N-MYC induced changes (Δ) in Pol II occupancy in control and in TFIIIC5-depleted cells.

B. Empirical distribution function (ECDF) plot showing changes in Pol II traveling ratio under the indicated conditions.

C. Metagene plot of all expressed genes (n=14,650) illustrating distribution of hypo-phosphorylated Pol II (8WG16) within transcribed regions before and five hours after activation of N-MYCER.

D. Occupancy of Pol II in the gene body (top) and at the TSS (bottom) sorted according to gene expression in IMR-5 cells synchronized in S phase and treated with CD532 where indicated. Only expressed genes were used (n=14,927) and 30 equal-sized bins (each representing 500 genes) were calculated using the arithmetic mean.

E. 2D Kernel density blot showing Pol II traveling ratio in S phase arrested cells after two hours of CD532 treatment before and after four hours of N-MYCER-activation.

F. Effect of Aurora-A inhibitors on phosphorylation of the indicated proteins in IMR-5 cells synchronized in S phase. Inhibitors were added for 2 hours in indicated concentrations (n = 4).

G. FACS analysis documenting altered DNA synthesis upon incubation of IMR-5 cells with MK- 5108, CD532 and MLN8237. Upper panels show BrdU/propidium iodide double staining (with BrdU-positive cells marked in green), lower panels show propidium iodide.